

An adaptive synchronous extraction (ASE) method for estimating intensity and footprint of surface urban heat islands: a case study of 254 North American cities

Qiquan Yang ^{a, b, c}, Yi Xu ^{a, *}, Xiaohua Tong ^{b, c, *}, Xin Huang ^{d, e, *}, Yue Liu ^f, TC Chakraborty ^g, Changjiang Xiao ^{b, c}, Ting Hu ^h

^a State Key Laboratory of Lunar and Planetary Sciences, Macau University of Science and Technology, Macau, China

^b College of Surveying & Geo-Informatics, Tongji University, Shanghai, 200092, China

^c The Shanghai Key Laboratory of Space Mapping and Remote Sensing for Planetary Exploration, Tongji University, Shanghai, 200092, China

^d School of Remote Sensing and Information Engineering, Wuhan University, Wuhan, 430079, China

^e State Key Laboratory of Information Engineering in Surveying, Mapping and Remote Sensing, Wuhan University, Wuhan, 430079, China

^f Guangzhou Institute of Geography, Guangdong Academy of Sciences, Guangzhou, 510070, China

^g Atmospheric Sciences and Global Change Division, Pacific Northwest National Laboratory, Richland, WA, USA

^h School of Remote Sensing and Geomatics Engineering, Nanjing University of Information Science and Technology, Nanjing, 210044, China

* Corresponding author. E-mail address: yixu@must.edu.mo (Yi Xu); xhtong@tongji.edu.cn (Xiaohua Tong); xhuang@whu.edu.cn (Xin Huang)

Abstract

The urban heat island (UHI) effect has attracted great attention due to its potential impacts on rapidly growing urban areas. Using remotely sensed estimates of land surface temperature (LST), a large number of studies have focused on the surface UHI (SUHI) effect, which can be characterized by its two fundamental properties: intensity and footprint. The SUHI intensity reflects the LST difference between the urban area and the background reference area (BRA), and the SUHI footprint indicates the spatial extent influenced by the heat island. Currently, numerous methods have been developed to estimate the SUHI intensity and footprint, but are still greatly challenged by three main issues. Namely, the discrepancy of BRA selection criterion brings great uncertainty to the SUHI intensity, the extraction of SUHI footprint is largely constrained by the predefined models, and the accuracy of SUHI indicators is potentially influenced by several confounding factors. Here, we proposed an adaptive synchronous extraction (ASE) method, which is capable of adaptively selecting the most optimal BRA while removing the influence of confounding factors, and achieving the synchronous estimation of SUHI intensity and footprint. We applied the ASE method to 254 North American cities and conducted an in-depth comparative analysis to discuss its applicability and benefits. The main results include: (1) The ASE method avoids the limitations of existing methods in BRA selection and model presetting, and shows resilience to parameter variations. This makes the ASE method highly applicable to quantify the SUHI intensity and footprint in cities with various thermal characteristics. (2) The ASE method can better highlight the spatial, seasonal and day-

night contrasts in the estimated SUHI intensity. This superiority is particularly evident when comparing it to methods based on the equal-area buffer or the simplified urban-extent algorithm. (3) Confounding factors pose non-negligible impacts on the quantification of the SUHI effect. Typically, ignoring the influence of topographic relief or LST data missing can lead to an overall overestimation of the SUHI intensity, while not removing surrounding urban areas will cause some underestimation of the SUHI intensity. Overall, the proposed ASE method provides a new generalizable tool for quantifying the SUHI effect, which has great potentials for future studies and urban climate assessments.

Keywords: Urban heat island effect; SUHI indicators; Urban-rural gradients; Land surface temperature; Spatiotemporal variations

1. Introduction

Urbanization can alter local thermal environment, causing urban areas to be warmer than their surroundings, a phenomenon known as the urban heat island (UHI) effect. The UHI effect can influence vegetation phenology, hydrologic cycle, and energy consumption in urban regions, and even pose a public health threat to urban dwellers (Jia et al. 2018; Li et al. 2019c; Wang et al. 2022; Ward et al. 2016; Zhou et al. 2018b; Zhou et al. 2016b). In view of continuing urban expansion and densification, as well as intensifying background climate change, the UHI effect and its potential impacts have attracted widespread attention.

Existing UHI studies can be broadly divided into those based on in-situ air temperature and those based on remotely sensed land surface temperature (LST). Remotely sensed LST has the advantage of easy access and high spatial resolution compared to in-situ air temperature, and therefore has been widely used in UHI studies in recent years (Zhou et al. 2018b). The LST-based UHI reflects the urban surface thermal environment and is therefore referred to as the surface UHI (SUHI) effect (Peng et al. 2012; Zhou et al. 2018b; Zhou et al. 2014). The primary research themes on SUHI can be divided into: quantitative methods, spatiotemporal patterns, influencing factors, and mitigation measures. Among them, the quantification of SUHI is foundational to tackle the other themes.

The most typical and widely studied property of the SUHI effect is its intensity (Schwarz et al. 2011; Zhou et al. 2018b). The SUHI intensity (SUHI_I) is generally defined as the average LST difference between an urban area and its background

reference area (BRA) (Li et al. 2022; Zhou et al. 2018b). Previous studies have widely regarded the fixed buffer ring outside urban extents as the BRA, but show difference in the size and location of the buffer ring (Chen et al. 2021; Cui et al. 2021; Hu et al. 2022; Huang et al. 2020; Lai et al. 2018; Lai et al. 2021a; Li et al. 2022; Liao et al. 2022; Manoli et al. 2019; Peng et al. 2012; Possega et al. 2022; She et al. 2021; Venter et al. 2021; Yang et al. 2017; Yao et al. 2019; Yao et al. 2018; Zhan et al. 2022; Zhou et al. 2014). There are two common methods for constructing buffer rings: distance-based methods and area-based methods. The distance-based methods construct the buffer ring (i.e., BRA) of a certain width (w) at a certain distance (d) away from the central urban area. However, both d and w differ greatly among existing studies, with a range of 0-50 km and 1-50 km, respectively (Li et al. 2019b). Obviously, differences in d and w can lead to large disparities in the selection of BRA, which in turn can have a significant impacts on the estimated SUHII (Li et al. 2019b). Moreover, the distance-based methods are also limited by the inapplicability of applying a single fixed buffer to cities of different sizes, especially in large-scale studies (Lai et al. 2018). The area-based methods determine the BRA as the neighboring buffer ring with an area that is a multiple ($0.5\times$, $1.0\times$, $1.5\times$, or others) of the corresponding urban area (Chakraborty et al. 2021; Lai et al. 2018; Lai et al. 2021a; Li et al. 2019b; Peng et al. 2012; Wang et al. 2015; Zhan et al. 2022). These methods take the size of the urban area into account when selecting the BRA, making it more suitable for the SUHI analysis across different cities. However, the area multiple used to determine the BRA is not standardized. To overcome the BRA selection difficulties of distance- and area-based methods,

Chakraborty and Lee (2019) developed a method based on the simplified urban-extent (SUE) algorithm (referred as SUE method here) to quantify the SUHII. This method distinguishes between urban areas and corresponding BRAs by land cover types, i.e., regarding built-ups as urban areas and other land covers (except water bodies) as BRAs. The SUE method gets rid of the difficulty of buffer selection, but may be challenged by the systematically lower SUHII due to the very close proximity of BRA to urban extents (Li et al. 2022).

Besides the intensity, the footprint is another fundamental property of the SUHI effect. The SUHI footprint (SUHIF) reflects the spatial extents influenced by the heat islands, and is an important indicator of the climatic impact of urbanization on the thermal environment (Hu et al. 2022; Streutker 2003; Yang et al. 2019; Zhou et al. 2015). According to the spatial distribution characteristics of urban LST (higher at the center or urban core and lower at the periphery), Streutker (2003) proposed a method to fit the urban LST by using the Gaussian model, and regarded the area under the fitted LST surface as the SUHIF. The Gaussian model's assumption of a single urban core oversimplifies the complexity of urban structure, leading to potential inaccuracies in fitting the LST variations within the city, particularly for cities with multiple urban cores (Quan et al., 2014; Yang et al., 2019). Zhang et al. (2004) demonstrated that the LST along urban-rural gradients followed a single exponential decay model. Based on this, Zhou et al. (2015) established multiple buffer rings centered on the urban area, and searched for the first buffer ring (from inside to outside) with mean LST statistically lower than that of the predefined BRA. The SUHIF is quantified as the area covered by

the selected buffer ring and its internal regions (including the urban area). Zhou et al. (2015) applied this method to 32 major Chinese cities and found that the SUHIF could be up to 6.5 times the size of the central urban area. This method provides a new approach for quantifying the footprint of SUHI effect, but is still limited by the selection of predefined BRA and cannot deal with the urban cool island effect (i.e., lower LST in urban areas). Later, Qiao et al. (2019) used the logistic algorithm to fit the urban-rural LST gradients in Beijing, and the SUHIF was automatically extracted through the curvature extremes of the fitted logistic curve. This approach has the advantage of automatic selection of BRA, but the universality of logistic algorithm for urban LST fitting is still inconclusive (Peng et al. 2020).

In addition to the methodology, the quantification of the SUHI effect requires attention to confounding factors. First, temperature is sensitive to local elevation, and the LST change caused by topographic relief (TR) can mask or amplify the SUHI effect, leading to bias in the SUHI indicators (Venter et al. 2021; Yao et al. 2018). To reduce the uncertainty caused by TR, a common practical method is to remove pixels with elevation anomalies (Cao et al. 2016; Chakraborty and Lee 2019; Chen et al. 2021; Yang et al. 2017; Yao et al. 2017; Zhao et al. 2014). Second, remotely sensed LST images usually suffer from missing values or large uncertainties due to the influence of clouds and shadows, which can have spatiotemporal dependencies (due to season, topography, coastal influences, etc.) , and thus introduce uncertainties for the SUHI indicators (Li et al. 2022). Large-scale seamless estimates of LST can be generated through spatiotemporal fusion techniques, which provides a feasible way to reduce the

bias caused by the missing data (Zhang et al. 2022). Third, the continued expansion of cities has resulted in an increasingly dense distribution of urban regions (Kuang et al. 2016; Zhou et al. 2018a). As a result, there are often other urban areas spread around a target city, leading to the SUHI of the target city being influenced by the surrounding urban areas (SUAs). More importantly, the influence of SUAs is often beyond the coverage of their physical boundaries, which has rarely been considered in existing studies.

In summary, existing studies have made important progress in estimating the two main SUHI indicators (SUHII and SUHIF), but still suffer from the following issues:

(1) The discrepancies between BRA selection criteria introduces uncertainties to the SUHII.

(2) The estimation of SUHIF is still limited by the predefined models.

(3) The accuracy of SUHI indicators can be influenced by several confounding factors.

To address the above issues, this study proposed an adaptive synchronous extraction (ASE) method to estimate the SUHII and SUHIF, which is capable of adaptively selecting the most optimal BRA while removing the influence of confounding factors, and simultaneously obtaining the intensity and footprint of the surface urban heat/cold island effect. Based on the ASE method, we analyzed the spatiotemporal patterns of SUHII and SUHIF in 254 North American cities (Figure 1), and further discussed the applicability of the proposed method through comparative analysis.

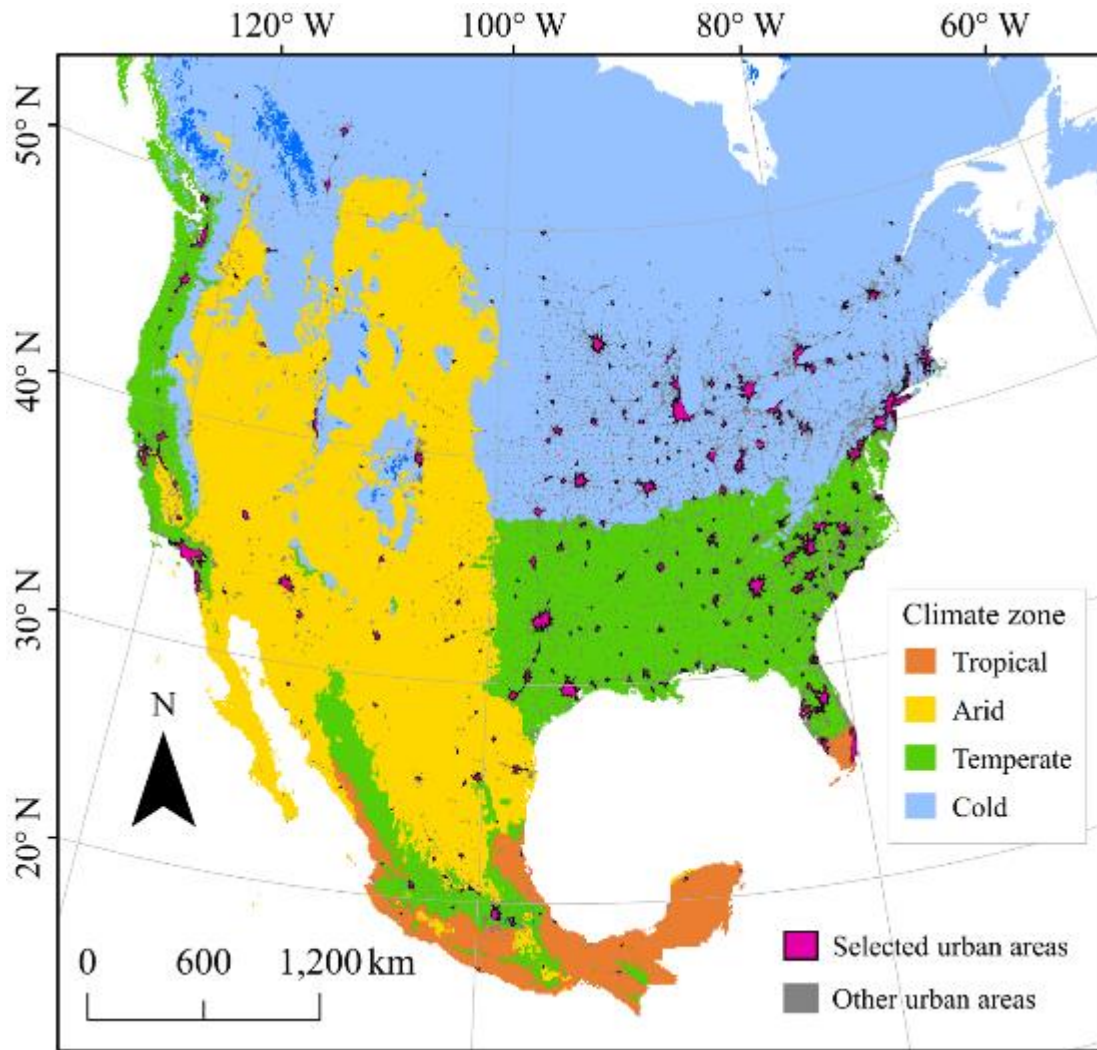


Figure 1. Spatial distributions of 254 North American cities and their urban extents. All cities are spatially distributed in four climate zones, including tropical (11 cities), arid (47 cities), temperate (111 cities) and cold (85 cities) zones. The climate zone boundaries are derived from the Köppen-Geiger climate subdivisions.

2. Data and methods

2.1 Data

The urban extents used in this study were from the global urban boundary (GUB) dataset (Li et al. 2020). This dataset provides high-resolution physical boundary of global urban areas for seven representative years (every five years from 1990 to 2015, and 2018), and the most recent year was chosen for this study. First, the original GUB

polygons within 2 kilometers (km) of each other were merged into the same urban cluster, and the threshold of 2 km is referred to previous studies (Lai et al. 2021b; Yang and Zhao 2023; Zhao et al. 2016; Zhou et al. 2014). Then, 254 spatially isolated urban clusters ($> 50 \text{ km}^2$) were selected over North America, with them being distributed across four different climate zones (tropical, arid, temperate, and cold) (Figure 1). The climate zones were derived from the major climate classes of the Köppen–Geiger climate scheme (Rubel and Kottek 2010).

Surface temperature observations were obtained from the seamless Moderate Resolution Imaging Spectroradiometer (MODIS) Aqua LST products produced by Zhang et al. (2022), which fills the missing values of the original MODIS LST (MYD11A1) by using a spatiotemporal gap-filling framework. Global-scale cross-validation indicates that the gap-filled LST dataset has good accuracy, with an average root mean squared error below than 2°C (Zhang et al. 2022). This gap-filled LST has been shown to be effective in analyzing the spatiotemporal patterns of the SUHI effect (Yang and Zhao 2023). Like the standard MODIS LST products, these gap-filled data can provide day-by-day daytime ($\sim 13:00$) and nighttime ($\sim 01:30$) LST observations with a spatial resolution of 1 km. We averaged the daily LST observations annually and seasonally, with June-August and December-February for summer and winter, respectively. The gap-filled LST can help to reduce uncertainties of the SUHI quantification caused by data missing (Li et al. 2022). In addition, we also included the original MODIS LST data (MYD11A1) for comparison to analyze the influence of data missing on the estimation of the SUHI effect. The original MODIS LST data have same

time ranges (2017-2019) and spatial extents (North America) as the gap-filled LST data, and were also annually and seasonally averaged, respectively.

The surface elevation was obtained from the Shuttle Radar Topography Mission (SRTM) digital elevation data with a spatial resolution of 1 km. This data was used to remove the influence of topographic relief on the SUHI indicators. All water pixels were removed according to the global surface water (GSW) produced by Pekel et al. (2016), which can provide the annually maximum water extent map (2017-2019) with a spatial resolution of 30 m. The land cover information was derived from the Copernicus Global Land Service (CGLS) product (2018), which has a spatial resolution of 100 m and an accuracy of 80% (Buchhorn et al. 2020). This product provides fractional estimates for basic land cover classes (built-ups, bare lands, trees, crops, shrubs, and grass), and was used to discuss the spatial variations of landcover change and its possible effect on the LST. Given the complexity of landcovers, we also included the 250 m-resolution MODIS enhanced vegetation index (EVI) product (MYD13Q1, 2017-2019) to describe the overall spatial variability of vegetation.

2.2 Estimation of SUHI intensity and footprint

As shown in Figure 2A, the most critical part of this study is the estimation of SUHII and SUHIF. According to previous studies (Manoli et al. 2019; Peng et al. 2018; Peng et al. 2012; Zhou et al. 2018b; Zhou et al. 2016a; Zhou et al. 2014), there are two typical spatial patterns of the LST from the urban core to the periphery: decreasing (i.e., urban heat island effect) and increasing (i.e., urban cold island effect). As the distance

from the urban area increases, the LST generally first shows a trend of rapid change (caused by urban-rural LST disparity) and then gradually levels off (approaching the rural mean LST) (Li et al. 2022; Li et al. 2019b). Therefore, there shall be a turning point (TP) from "rapid change" to "leveling off" for the urban-rural LST gradients (Figure 2B), and the area where the TP is located can be considered to be the most optimal BRA to use for quantifying the SUHI effect. On this basis, we proposed a so called adaptive synchronous extraction (i.e., ASE) method, which is capable of adaptively extracting the most optimal BRA based on the continuous characteristics of urban-rural LST gradients, and thus achieving the synchronous estimation of SUHI and SUHIF. As shown in Figure 2B, The ASE method consists of three main steps: delineation of potential BRAs, selection of the most optimal BRA, and calculation of the SUHI and SUHIF.

2.2.1 Delineation of potential BRAs

The selection of BRA is the key to quantifying the SUHI effect. Before selecting the most optimal BRA, we first obtained all the possible regions of BRAs (referred to as potential BRAs) by spatial analysis, which mainly includes the following operations.

(1) Constructing multiple equal-area buffers

For each target city, the urban cluster obtained from the GUB data was regarded as the center urban area. We created twenty buffers outward from the central urban area, and ensured that each buffer was half the size of the central urban area. Thus, the area covered by the outermost buffer and its inner regions reaches 11 times the central urban

area, far exceeding the upper bound of the SUHI footprint (6.5 times of the central urban area) proposed by a previous national-scale study over China (Zhou et al. 2015). It is reasonable to believe that the optimal BRA we are searching for is within the area covered by the constructed buffers (Figure 2B2). Here more attentions should be paid to the size of the constructed buffers outside the central urban area. Choosing a smaller size requires creating more buffers, which will cause a greater burden on data processing and computation; while choosing a large size will cause a loss of precision of the estimated SUHIF given the way SUHIF is calculated (see section 2.2.3). After weighing the pros and cons, we set the size of each buffer ($\text{Buffer}_{\text{size}}$) to 1/2, i.e., half the size of the central urban area, which was also adopted by previous studies (Huang et al. 2019; Zhou et al. 2015). In addition, we also set the $\text{Buffer}_{\text{size}}$ to other values and tested the sensitivity of our results to the $\text{Buffer}_{\text{size}}$ (see section 3.4).

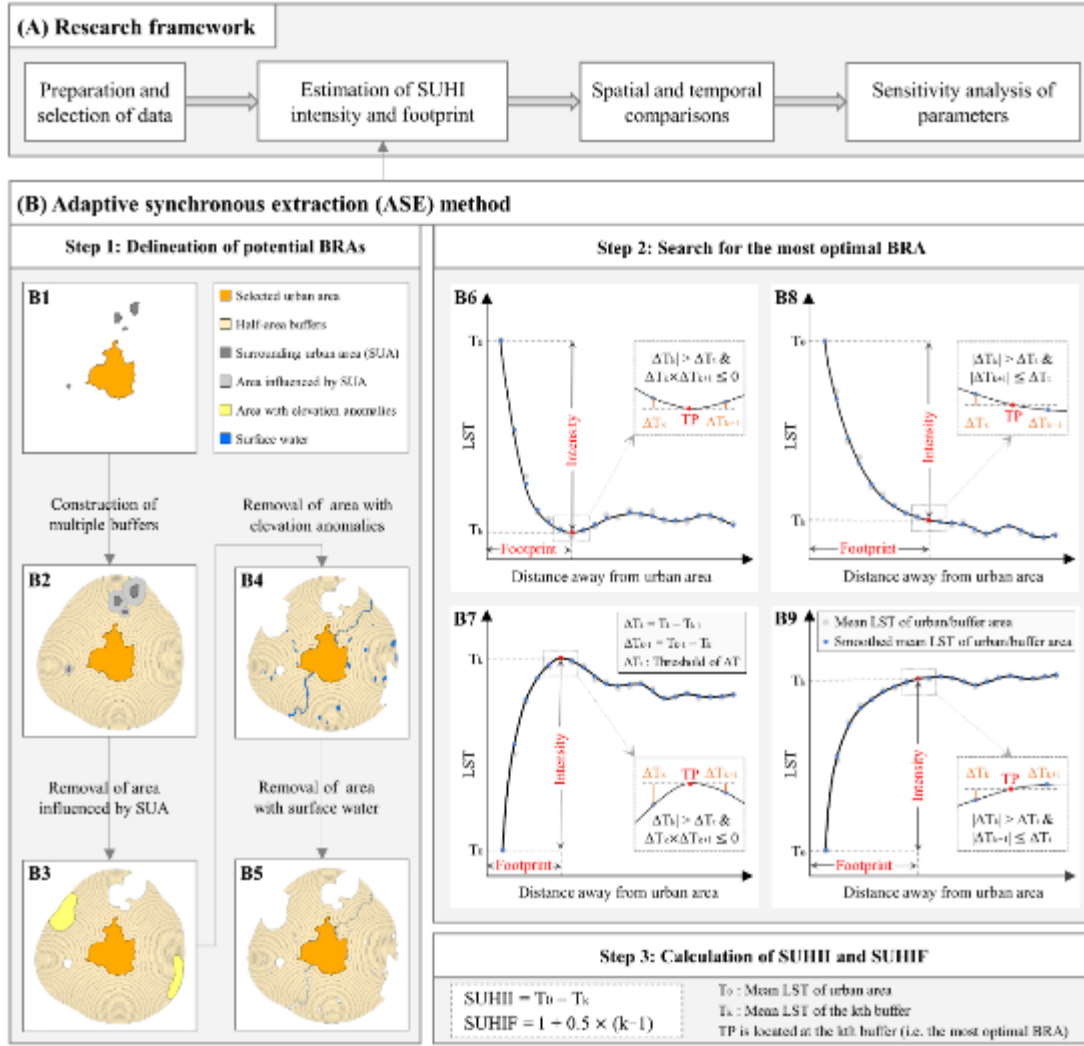


Figure 2. Schematic diagram of the framework and methodology of this study. TP refers to the turning point of urban-rural LST gradients, located at the buffer of the most optimal background reference area (BRA). SUHII and SUHIF refer to intensity and footprint of surface urban heat islands, respectively.

(2) Removing regions influenced by surrounding urban areas

Due to the increasing density of urban distribution, there may be other urban areas distributed nearby the target urban area. We obtained other urban areas around the target urban area based on the urban clusters of the GUB data, and referred to these other urban areas as the surrounding urban areas (SUAs). The SUAs could disturb the LST distribution around the target city, and further influence the search for the optimal BRA.

It is, therefore, necessary to remove the influence of SUAs before quantifying the SUHI effect. Considering that the SUHI effect can transcend the physical boundaries of urban extents (Zhang et al. 2004; Zhou et al. 2015), we need to remove not only the regions covered by the SUAs themselves, but also the regions they possibly radiate to. Thus, we enlarged each SUA equidistantly to the outside, until its area reached the previously reported the upper bounds of the SUHI footprint (i.e., 6.5 times of each SUA). After that, for each target city, we removed all the regions covered by the expanded SUAs around it (Figure 2B3). This study enlarged the SUA by 6.5 times, and this stringent criterion can help to remove the influence of SUA as much as possible. We also tested the sensitivity of our results to the size of SUA (noted as SUA_{size}), and see section 3.4 for details.

(3) Removing regions disturbed by topographic reliefs

Considering high sensitivity of LST to elevation, it is necessary to remove regions influenced by topographic relief before quantifying the SUHI effect. Referring to previous studies (Imhoff et al. 2010; Lai et al. 2018; Venter et al. 2021; Yang and Zhao 2023), we first calculated the urban average elevation (E_{Ave}) of the central urban area, and then removed regions that were too high ($> E_{Ave} + E_t$) or too low ($< E_{Ave} - E_t$) in the surrounding buffers (Figure 2B4). The E_t was customarily set to a strict threshold of 50 m (Imhoff et al. 2010; Lai et al. 2018; Venter et al. 2021; Yang and Zhao 2023), and this usual threshold was also adopted by this study. Besides, the sensitivity of our results to E_t was also tested (see section 3.4).

Besides the above steps, regions covered by water bodies were also removed, and

the remaining regions of the surrounding buffers were regarded as potential BRAs (Figure 2B5).

2.2.2 Selection of the most optimal BRA

Based on the potential BRAs obtained in the previous step, we first calculated the mean LST of urban area and surrounding buffers, and then minimized fluctuations in data using the cubic smoothing spline method (De Boor and De Boor 1978). This smoothing operation can reduce the influence of local LST anomalies on its overall patterns, and highlight the continuous characteristics of urban-rural LST gradients. For a given city, we assumed that the set formed by the smoothed mean LST is $\mathbf{T} = (T_0, T_1, T_2, \dots, T_{20})$, where T_0 is the smoothed mean LST of urban area, and T_1 to T_{20} are the smoothed mean LST of outer buffers (outward from the central urban area). We calculated the difference of adjacent elements (the latter minus the former) of the set \mathbf{T} , and obtained a new set $\Delta\mathbf{T} = (\Delta T_1, \Delta T_2, \dots, \Delta T_{20})$, where $\Delta T_i = T_i - T_{i-1}$ ($i \in [1, 2, \dots, 20]$). Obviously, according to the general pattern of urban-rural LST gradients, the absolute value of ΔT_i (i.e., $|\Delta T_i|$) will decrease with the increment of i until it levels off. Therefore, we compared $|\Delta T_i|$ with a certain threshold (assumed to be ΔT_t) until one of the following occurs:

(1) When i increases to k ($k \in [1, 2, \dots, 20]$), satisfying $|\Delta T_k| > \Delta T_t$ & $\Delta T_k \times \Delta T_{k+1} \leq 0$. As shown in Figure 2 B6&B7, there shall be a point near T_k where the curvature of the smoothed LST curve equals to zero, and the k th buffer corresponds to the most optimal BRA we are searching for.

(2) When i increases to k ($k \in [1, 2, \dots, 20]$), satisfying $|\Delta T_k| > \Delta T_t$ & $|\Delta T_{k+1}| \leq \Delta T_t$.

The corresponding cases are shown in Figure 2 B8&B9, and the most optimal BRA shall be within the k th buffer.

The threshold ΔT_t is determined as:

$$\Delta T_t = \text{Per}_t \times (T_{\max} - T_{\min}) \quad (1)$$

where T_{\max} and T_{\min} are the maximum and minimum values in the set T , respectively, and Per_t is a scaling factor. This approach makes the ΔT_t closely related to the LST range of the city itself, avoiding the uncertainty caused by using a fixed threshold. Referring to Alkama and Cescatti (2016), here the scaling factor Per_t is set to 2%, and the sensitivity of our results to Per_t is presented in section 3.4.

2.2.3 Calculation of SUHI intensity and footprint

With the above steps, we can find the most optimal BRA. For a given urban area, assuming that the most optimal BRA is located at the k th buffer, then the SUHI intensity (SUHII) and footprint (SUHIF) can be calculated as:

$$\text{SUHII} = T_0 - T_k \quad (2)$$

$$\text{SUHIF} = \begin{cases} 1, & k < 2 \\ 1 + \sum_{i=1}^{k-1} F_i, & k \geq 2 \end{cases} \quad (3)$$

Where T_0 is the mean LST of urban area, and T_k is the smoothed mean LST of the k th buffer. F_i refers to the ratio of the size of the i th buffer to the size of the central urban area. Positive/negative SUHII indicates urban heat/cold island effect. SUHIF refers to the ratio of the area affected by the SUHI effect to the area of the central urban. In this study, the area of each buffer is half the size of the urban area (i.e., $F_i = 0.5$), so the

formula for SUHIF can be simplified as:

$$\text{SUHIF} = 1 + 0.5 \times (k - 1) \quad (4)$$

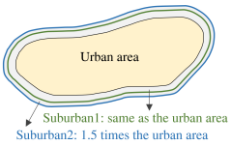

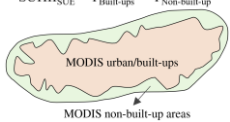
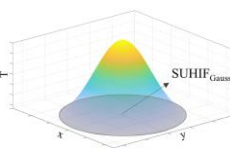
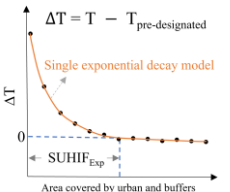
2.3 Comparative analysis of methods

To highlight the validity and advantages of the ASE method, we compared it with the SUHI indicators obtained by previous methods. As shown in Table 1, five SUHI indicators ($\text{SUHI}_{\text{Sub1}}$, $\text{SUHI}_{\text{Sub2}}$, $\text{SUHI}_{\text{Rur1}}$, $\text{SUHI}_{\text{Rur2}}$, SUHI_{SUE}) and two SUHIF indicators ($\text{SUHIF}_{\text{Gauss}}$, $\text{SUHIF}_{\text{Exp}}$) were included for comparison.

$\text{SUHI}_{\text{Sub1}}$ and $\text{SUHI}_{\text{Sub2}}$ were derived from area-based methods, defined as the average LST differences between urban areas and suburban1 (the neighboring buffer ring with equal size as the central urban area) and suburban2 (the neighboring buffer ring 1.5 times the size of the central urban area), respectively (Peng et al. 2012; Yang et al. 2017; Zhou et al. 2014). $\text{SUHI}_{\text{Rur1}}$ and $\text{SUHI}_{\text{Rur2}}$ were derived from distance-based methods, defined as the average LST differences between urban areas and rural1 (the 20 km wide buffer ring located between 10 and 30 km away from the central urban area) and rural2 (the 5 km wide buffer ring located between 45 and 50 km away from the central urban area), respectively (Imhoff et al. 2010; Yao et al. 2019). SUHI_{SUE} was estimated by the simplified urban-extent (SUE) algorithm, defined as the average LST difference between the MODIS urban/built-ups and the other landcovers within the urban extent (Chakraborty and Lee 2019). In the estimation of SUHIF, Streutker (2003) proposed that the spatial distribution of urban LST can be fitted by a three-dimensional Gaussian surface, and the SUHIF is determined by the area under the surface of the

fitted LST. Besides, Zhou et al. (2015) found that the urban-rural LST gradient fits well with a single exponential decay model, and the SUHIF can be estimated as the coverage with mean LST statistically larger than that of pre-designated rural reference areas. The SUHIF obtained by the above two methods were divided by the area of central urban, and the corresponding ratios were noted as $SUHIF_{Gauss}$ and $SUHIF_{Exp}$.

Table 1. SUHI indicators used for method-comparison analysis

Indicators	Descriptions and illustrations	
SUHI intensity (SUHI)		
SUHI _{Sub1}	Mean LST difference between urban area and surrounding suburban area (same as the urban area, referred as suburban1) (Yang et al. 2017; Zhou et al. 2014).	$SUHI_{Sub1} = T_{Urban} - T_{Suburban1}$ $SUHI_{Sub2} = T_{Urban} - T_{Suburban2}$ 
SUHI _{Sub2}	Mean LST difference between urban area and surrounding suburban area (1.5 times the urban area, referred as suburban2) (Peng et al. 2012).	
SUHI _{Rur1}	Mean LST difference between urban area and rural area (20 km wide ring located between 10 and 30 km away from the urban area, referred as rural1) (Yao et al. 2019).	$SUHI_{Rur1} = T_{Urban} - T_{Rural1}$ $SUHI_{Rur2} = T_{Urban} - T_{Rural2}$ 
SUHI _{Rur2}	Mean LST difference between urban area and rural area (5 km wide ring located between 45 and 50 km away from the urban area, referred as rural2) (Imhoff et al. 2010).	
SUHI _{SUE}	SUHI _{SUE} is quantified by a simplified urban-extent (SUE) algorithm, defined as mean LST difference between the MODIS urban/built-ups and other landcovers within urban extents (Chakraborty and Lee 2019).	$SUHI_{SUE} = T_{Built-ups} - T_{Non-built-up}$ 
SUHI footprint (SUHIF)		
SUHIF _{Gauss}	The urban LST can be modelled by a Gaussian model, and the SUHIF is determined by the area under the surface of the fitted LST. (For comparison purposes, it is divided by the area of central urban) (Streutker 2003; Yang et al. 2019).	
SUHIF _{Exp}	The urban-rural LST gradient is assumed to follow a single exponential decay model, and the SUHIF is defined as the coverage with mean LST (T) statistically larger than that of pre-designated rural reference areas (T _{pre-designated}) (For comparison purposes, the area is divided by the area of central urban) (Zhou et al. 2015).	$\Delta T = T - T_{pre-designated}$ 

We calculated all the above SUHI indicators for 254 North American cities using the same data and processing as the ASE method. Then, we analyzed the spatial patterns, seasonal variations and day-night differences of all the SUHI indicators and compared them with the results of the ASE method.

2.4 Analysis of confounding factors and parameters

2.4.1 Influence of confounding factors

The estimation of SUHII and/or SUHIF can be influenced by confounding factors, including topographic relief (TR), surrounding urban areas (SUAs), and LST data missing (DM). We quantified the influence of these factors on the estimated SUHII and/or SUHIF through the following comparative analysis: (1) Removal of areas disturbed by TR vs. no removal of areas disturbed by TR; (2) Removal of areas disturbed by SUAs vs. no removal of areas disturbed by SUAs; (3) Using the gap-filled MODIS LST data vs. using the original MODIS LST data. We performed the above comparative experiments separately for each method, and compared the obtained SUHII and/or SUHIF across North American cities.

2.4.2 Sensitivity tests of parameters

The ASE method mainly involves four parameters, including $Buffer_{size}$, SUA_{size} , E_t , and Per_t . The first three parameters are those involved in the delineation of potential BRAs (step 1 of the ASE method), and Per_t is the key parameter for finding the most optimal BRA (step 2 of the ASE method). The definitions and roles of all the parameters

have been described in section 2.2. To test the sensitivity of our results to these parameters, we compared the SUHII and SUHIF obtained under different values of each parameter. A brief description of all parameters, along with their default values (the values used in this study) and their values in the sensitivity tests, is presented in Table 2. It should be emphasized that when we performed the sensitivity test for a parameter, the other parameters remained at their default values.

Table 2. Parameters and their values in the ASE method

Parameters	Descriptions	Default values	Values for sensitivity tests
Buffer _{size}	The ratio of the size of each buffer to the size of the central urban area	1/2	1/4, 1/3, 2/3, 3/4
E _t	Elevation threshold for removing the influence of topographic relief	50 m	100 m, 150 m, 200 m
SUA _{size}	The multiple by which the size of the surrounding urban area is expanded	6.5	2.0, 3.5, 5.0
Per _t	A scaling factor determining the threshold for the extraction of turning points	2%	1%, 3%, 4%, 5%, 6%

3. Results

3.1 Turning points and background reference areas

As shown in Figure 3A, the ASE method can adaptively extract the turning points (TPs) of urban-rural LST gradients. The urban-rural LST curves vary by city and time, resulting in changes in TPs for 254 North American cities (Figure 3B). The locations of annual daytime and nighttime TPs are away from the urban area by a distance of 1.0 to 6.5 times the size of urban area (Figure 3B). The buffer at the location of TP is regarded as the background reference area (BRA) obtained by the ASE method, and the BRAs of different methods show large differences (Figure 3A). Compared with the BRA

extracted by the ASE method, the BRAs of area-based methods (suburban1 and suburban2) are mostly closer to the central urban area (Figure 4A), while the BRAs of distance-based methods (rural1 and rural2) are generally farther away from the urban area (Figure 4B). The difference in BRA can cause discrepancies in the estimated SUHII (see the next section), given the variation in urban-rural LST curves (Figure 3).

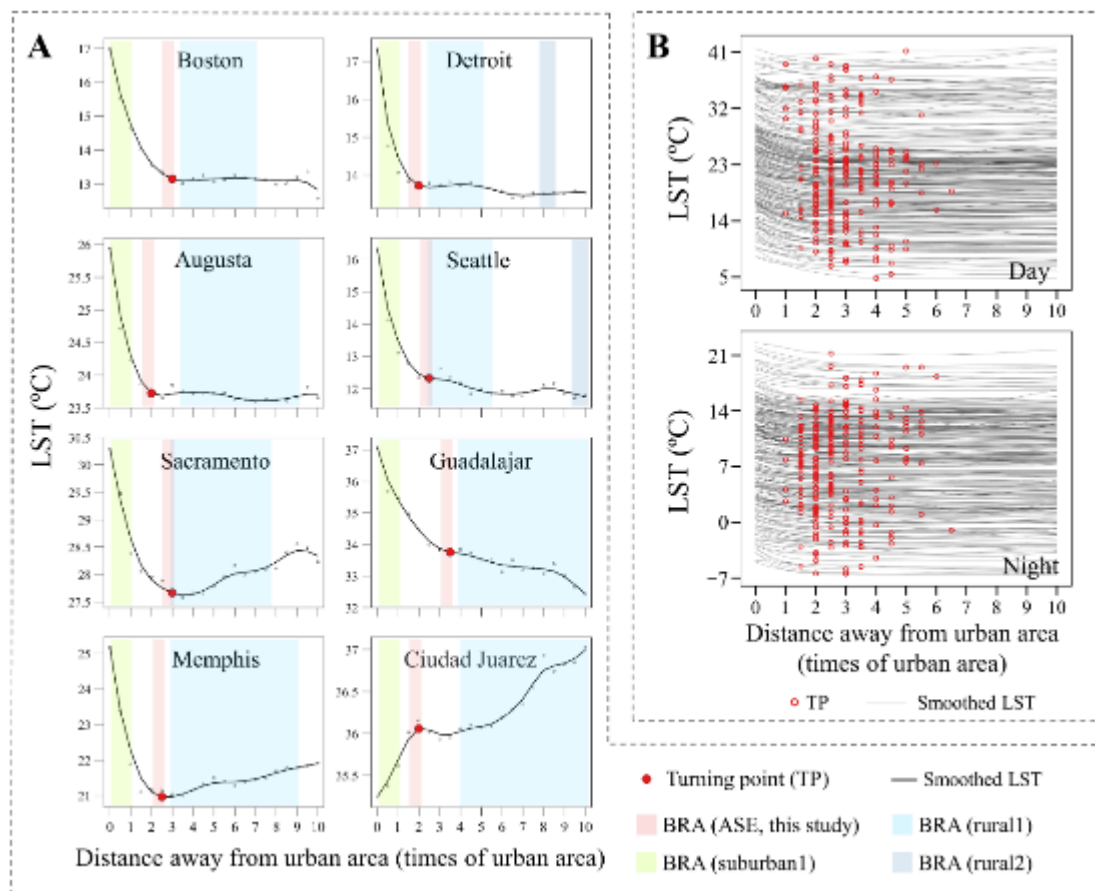


Figure 3. The turning point (TP) of the urban-rural LST gradient extracted by the ASE method. (A) The TP and its comparison with the background reference area (BRA) of different methods, an example of 8 typical cities. Suburban2 is not shown because it overlaps with suburban1 for the most part. Rural2 is not shown for some cities because they are too far from the urban area to be displayed. (B) The TPs of annual daytime and nighttime urban-rural LST gradients extracted by the ASE method in 254 North American cities.

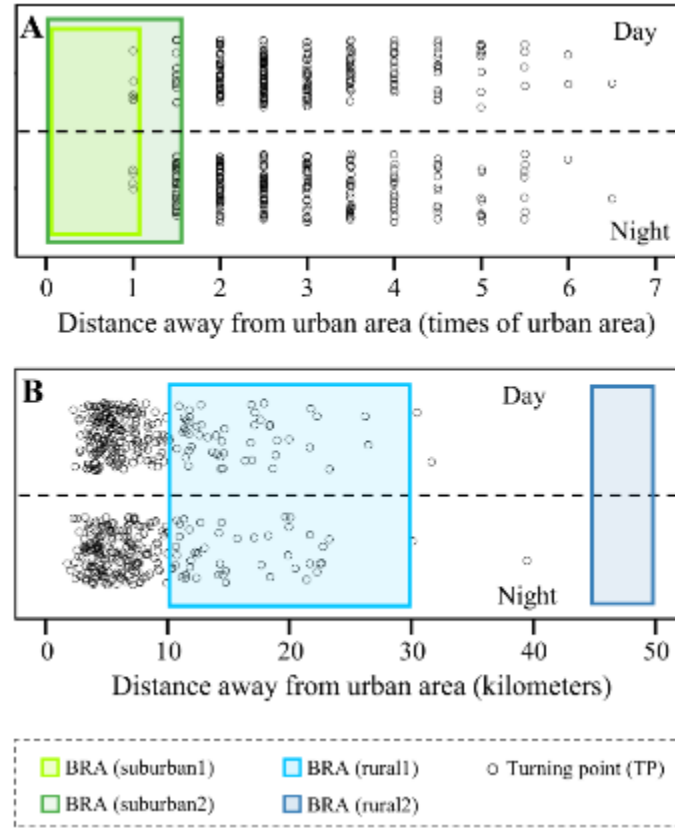


Figure 4. Comparison of the turning point (TP) extracted by the ASE method with the background reference area (BRA) of other methods. (A) Comparison of the TP with the BRA of area-based methods (suburban1 and suburban2). (B) Comparison of the TP with the BRA of distance-based methods (rural1 and rural2).

3.2 SUHI intensity and footprint

3.2.1 SUHI intensity

Figures 5-6 shows the spatial distribution of annual daytime and nighttime SUHII across 254 North American cities. The SUHII obtained by different methods has similar spatial patterns, and arid cities whiteness averagely lowest annual daytime SUHII and highest annual nighttime SUHII (Figures 5-6). However, there are differences in the specific value and the degree of spatial variation of SUHII for different methods. The SUHII estimated by the ASE method (i.e. $SUHII_{ASE}$) is overall higher and has a stronger spatial variation than the SUHII obtained by other methods (Figures 5-6). The mean

annual daytime $SUHII_{ASE}$ for the tropical and arid zones, for example, reaches 3.36 ± 0.82 °C (95% confidence interval, hereafter) and 0.91 ± 0.48 °C, respectively, and their values and differences are stronger than those of the other methods, especially the $SUHII_{SUE}$ (1.40 ± 0.5 °C and 0.58 ± 0.17 °C) (Figure 5B).

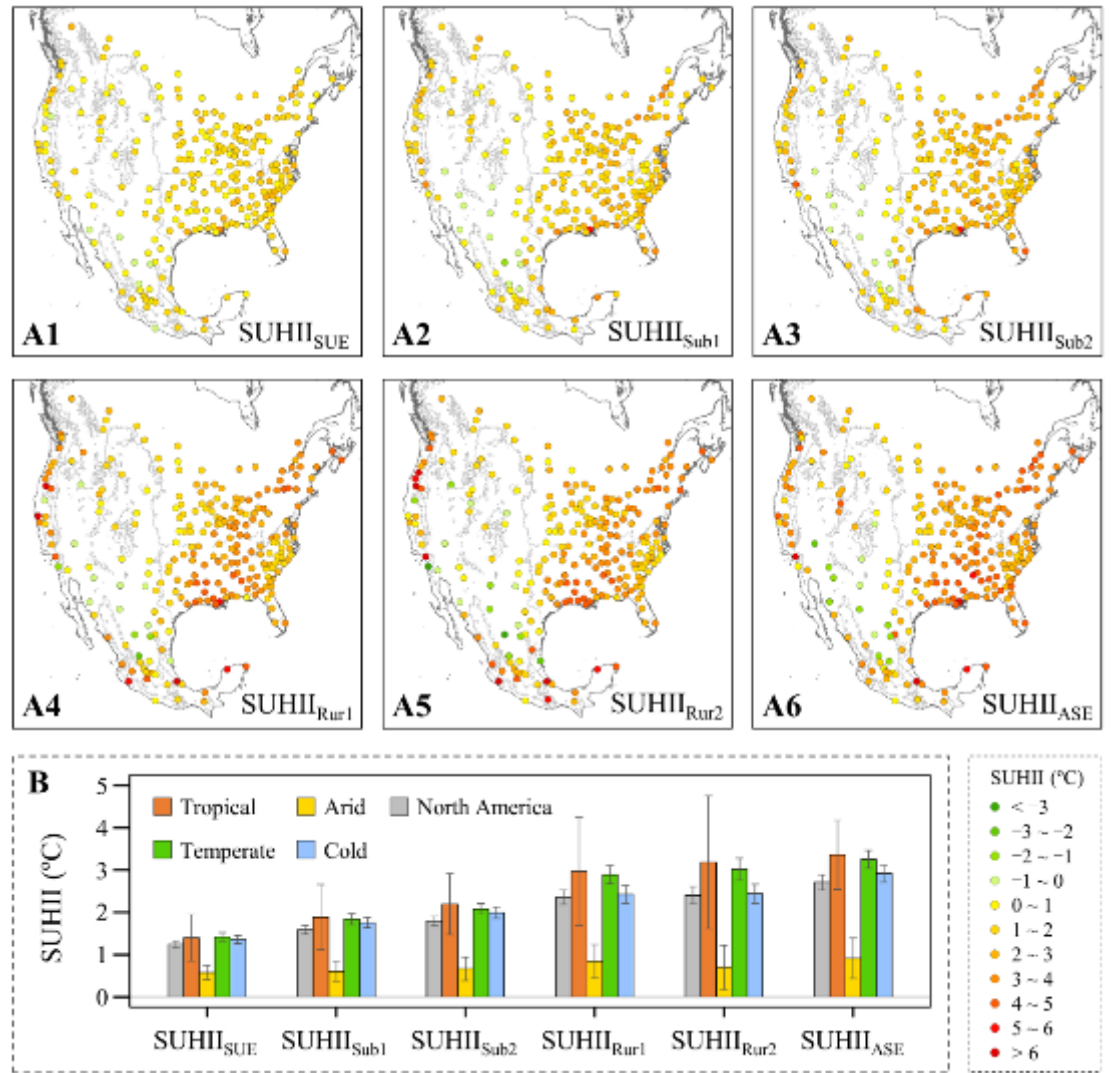


Figure 5. Spatial contrast of the annual daytime SUHI intensity (SUHII) obtained by different methods. (A) Spatial variation of the annual daytime SUHII across 254 North American cities. (B) Mean (\pm 95% confidence interval) of the annual daytime SUHII.

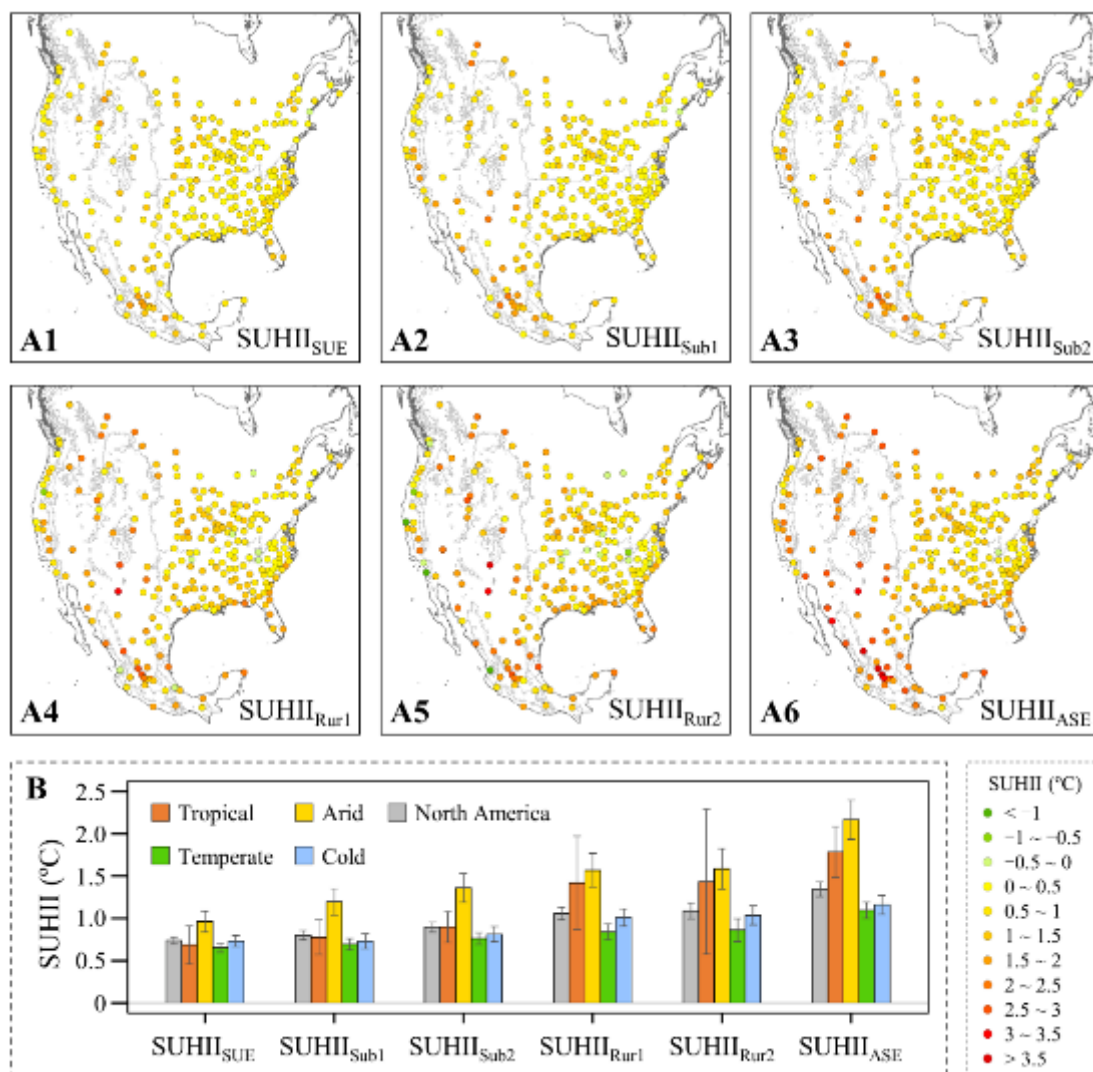


Figure 6. Spatial contrast of the annual nighttime SUHII intensity (SUHII) obtained by different methods. (A) Spatial variation of the annual nighttime SUHII across 254 North American cities. (B) Mean (\pm 95% confidence interval) of the annual nighttime SUHII.

Figure 7 illustrates the day-night and summer-winter contrasts in the SUHII. The SUHII quantified by all methods shows a consistent pattern, with higher values during the day than at night (except for the arid zone) and higher values in summer than in winter on average (Figure 7). However, compared to other methods, the SUHII estimated by the ASE method exhibits stronger day-night and summer-winter contrasts. Specifically, the day-night (or summer-winter) difference in SUHII_{ASE} is on average

about 2-4 times, 1.5-3 times and 1.0-1.5 times greater than those in $SUHII_{SUE}$, $SUHII_{Sub1/2}$ and $SUHII_{Rur1/2}$, respectively (Figure 7).

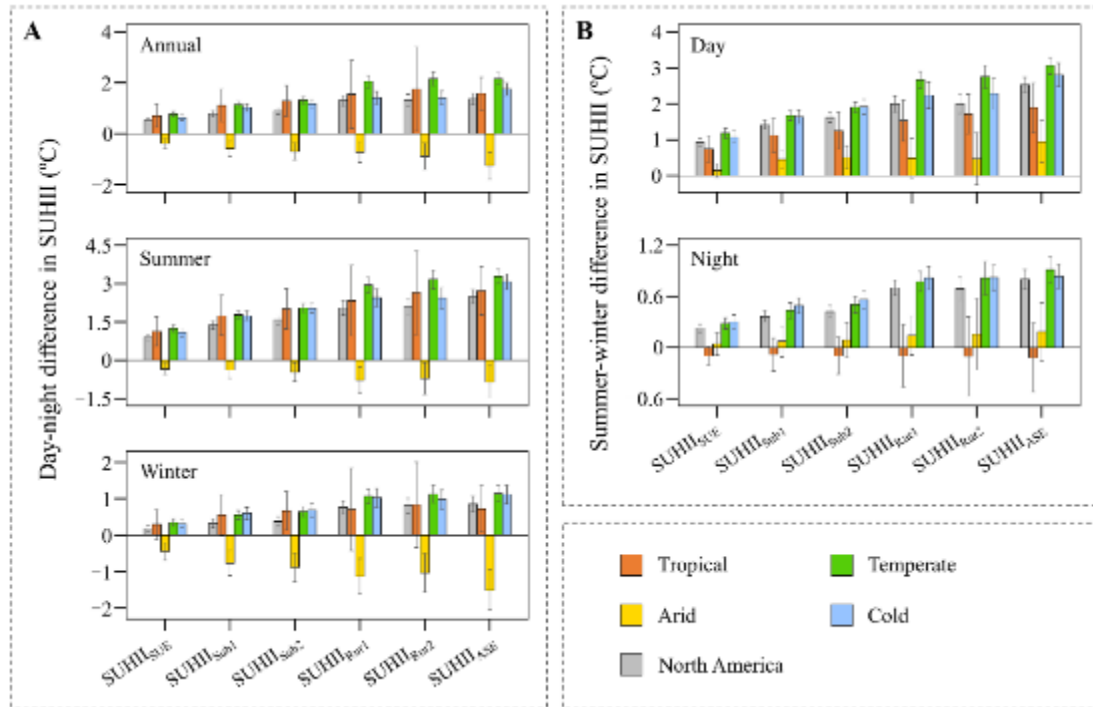


Figure 7. Day-night and winter-summer contrasts in the SUHI intensity (SUHII) for different methods. (A) Day-night difference in the SUHII. (B) Winter-summer difference in the SUHII. The histograms and bars represent the mean values and 95% confidence intervals, respectively.

3.2.2 SUHI footprint

Figure 8 depicts the spatial distribution of annual daytime and nighttime SUHIF for 254 North American cities. Unlike the SUHII, the SUHIF is more evenly distributed across climate zones. Compared with the $SUHIF_{ASE}$ (i.e., SUHIF obtained by the ASE method), the $SUHIF_{Gauss}$ tends to be smaller and has lower spatial variability (Figure 8A), while the $SUHIF_{Exp}$ appears to be higher and has stronger spatial heterogeneity (Figure 8B). Besides, Gaussian and exponential models fail to extract the SUHIF in some cities, resulting in null values of $SUHIF_{Gauss}$ and $SUHIF_{Exp}$ (Figure 8A&B).

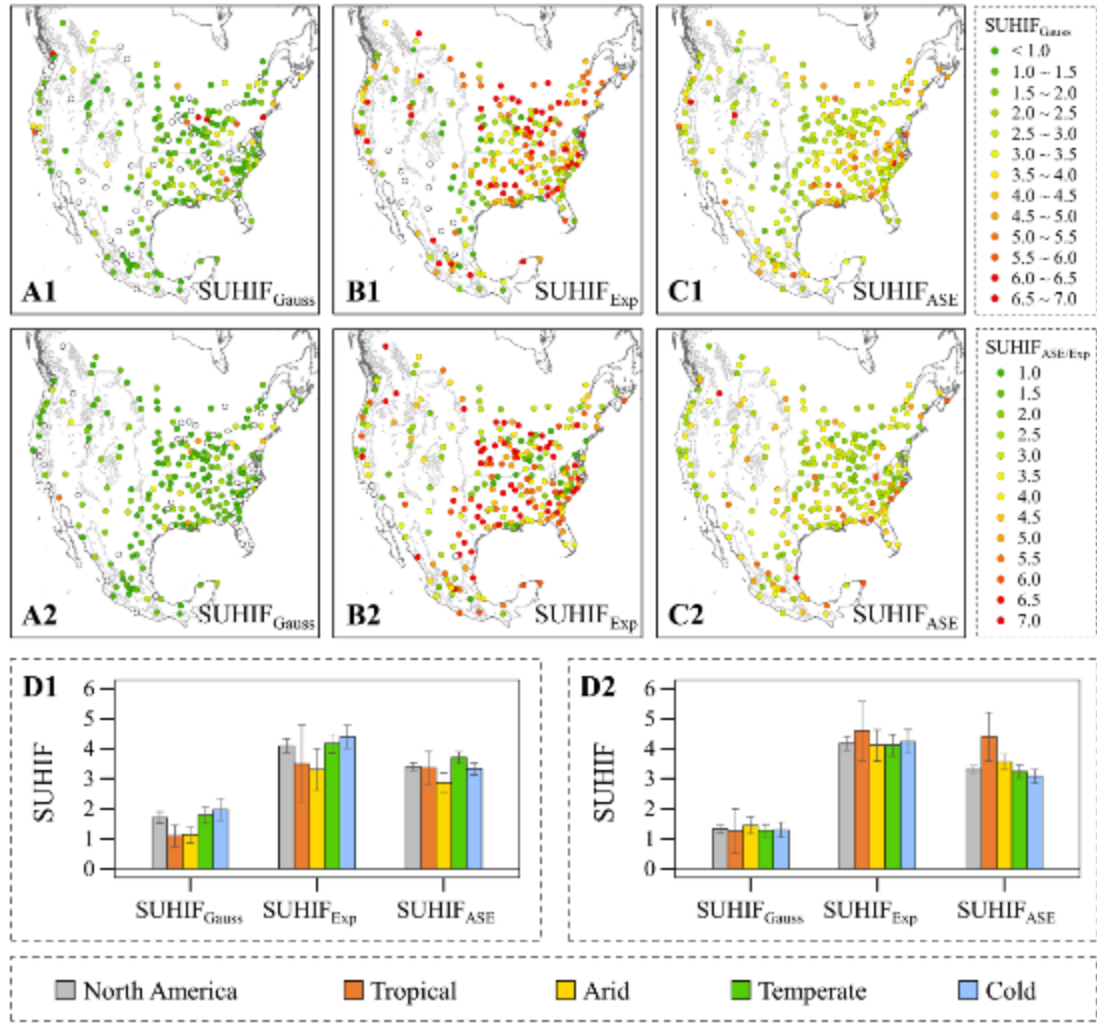


Figure 8. Spatial contrast of the SUHI footprint (SUHIF) obtained by different methods. (A-C) Spatial variation of the SUHIF across 254 North American cities. The hollow circles indicate the SUHIF that failed to be estimated by the model-based methods (Gaussian or exponential model). (D) Mean (\pm 95% confidence interval) of the SUHIF. (A1-D1) Annual daytime SUHIF. (A2-D2) Annual nighttime SUHIF.

As shown in Figure 9, the SUHIF obtained by different methods is generally consistent in terms of day-night and summer-winter variations. On average, daytime SUHIF is higher than nighttime SUHIF in temperate and cold zones, and lower than nighttime SUHIF in tropical and arid zones (Figure 9A). In terms of seasonal contrast, SUHIF is on average stronger in summer than in winter (Figure 9B). However, in most cases, the day-night and summer-winter differences in SUHIF are not statistically

significant at the 95% confidence interval (Figure 9).

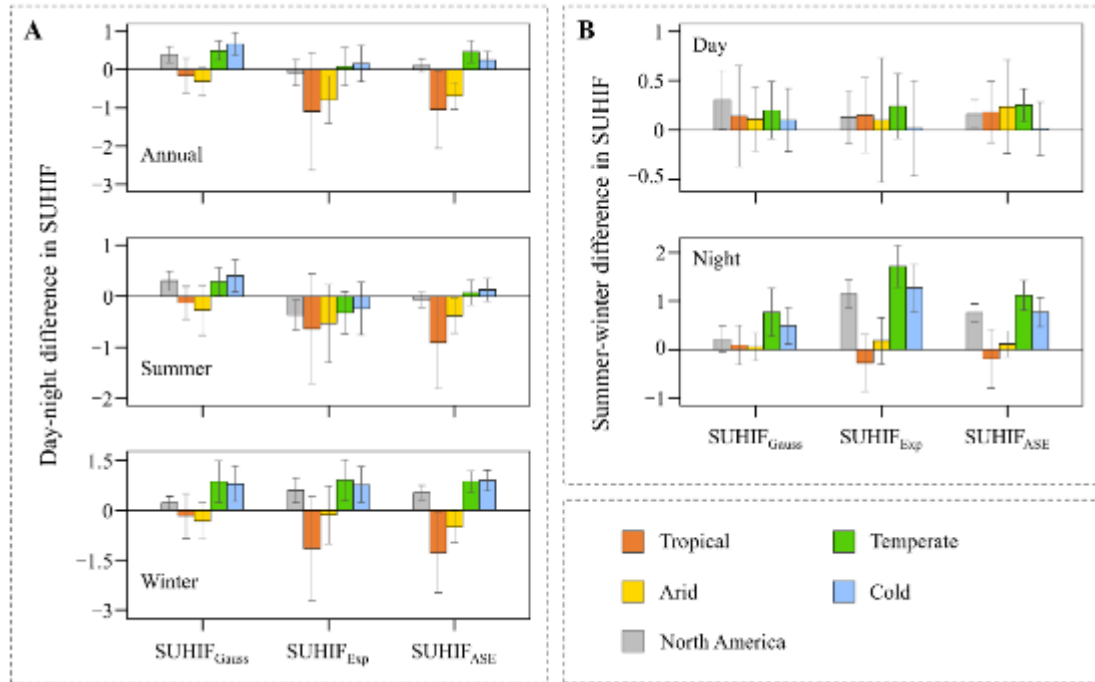


Figure 9. Day-night and winter-summer contrasts in the SUHI footprint (SUHIF) for different methods. (A) Day-night difference in the SUHIF. (B) Winter-summer difference in the SUHIF. The histograms and bars represent the mean values and 95% confidence intervals, respectively.

3.3 Influence of confounding factors

The LST around urban areas can be disturbed by the topographic relief (TR) and the surrounding urban areas (SUAs), leading to bias in the estimated SUHII and SUHIF of the ASE method (Figure S1). About half of the cities were influenced by TR, which is comparable to the number of cities disturbed by SUAs (Figure S1). We performed comparative analysis (see section 2.4.1) for cities influenced by TR and SUAs, respectively. It is found that ignoring the influence of TR can lead to an overall overestimation of the SUHII_{ASE} and SUHIF_{ASE} (Figure 10A), while not removing SUAs will cause some underestimation of the SUHII_{ASE} and SUHIF_{ASE} (Figure 10B). More importantly, TR and SUAs have similar effects on the SUHII and SUHIF estimated by

other methods, albeit to a different extent (much weaker for $SUHII_{SUE}$ and $SUHIF_{Gauss}$) (Figure 11A&B).

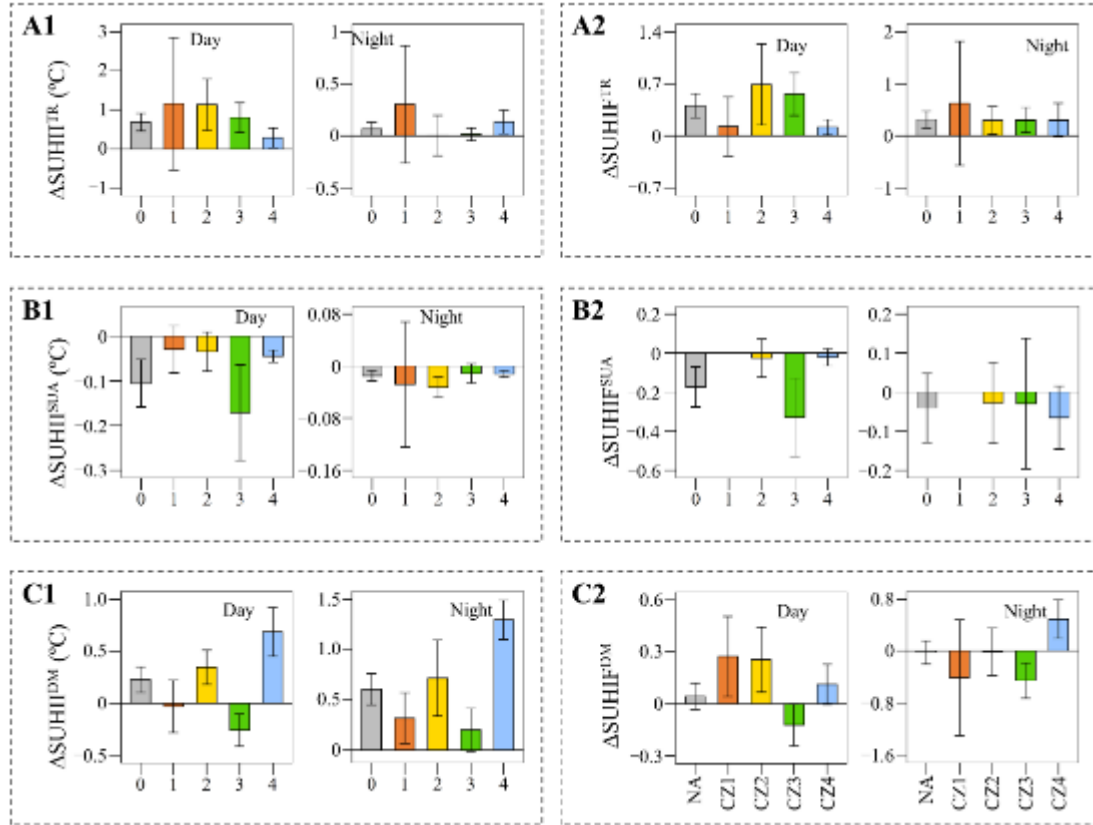


Figure 10. Influence of confounding factors on the SUHI intensity (SUHII) and footprint (SUHIF) estimated by the ASE method. (A) The average difference in the SUHII ($\Delta SUHII^{TR}$) or SUHIF ($\Delta SUHIF^{TR}$) between that disturbed by topographic relief (TR) and that removed the influence of TR. (B) The average difference in the SUHII ($\Delta SUHII^{SUA}$) or SUHIF ($\Delta SUHIF^{SUA}$) between that disturbed by surrounding urban areas (SUAs) and that removed the influence of SUAs. (C) The average difference in the SUHII ($\Delta SUHII^{DM}$) or SUHIF ($\Delta SUHIF^{DM}$) between that estimated by the original MODIS LST data (disturbed by data missing (DM)) and that estimated by the gap-filled MODIS LST data. NA, CZ1, CZ2, CZ3 and CZ4 represent North America, tropical zone, arid zone, temperate zone and cold zone, respectively. The histograms and bars represent the mean values and 95% confidence intervals, respectively.

In addition, the original MODIS daily LST observations (MYD11A1) are severely missing in cities, with an average missing rate of nearly 60% (Figure S2). The mean LST, as well as the SUHII and SUHIF, based on the original LST data, differs from

those by using the gap-filled LST data (Figures S2-S3). The SUHII obtained from the original MODIS LST data is on average higher than that derived from the gap-filled LST data (Figure 10C). Such difference caused by data missing (DM) has been observed for the SUHII estimated by different methods (Figure 11C). In addition, the effect of DM on SUHIF shows high spatial heterogeneity and differs across methods (less effect on $SUHIF_{Gauss}$) (Figure 11C).

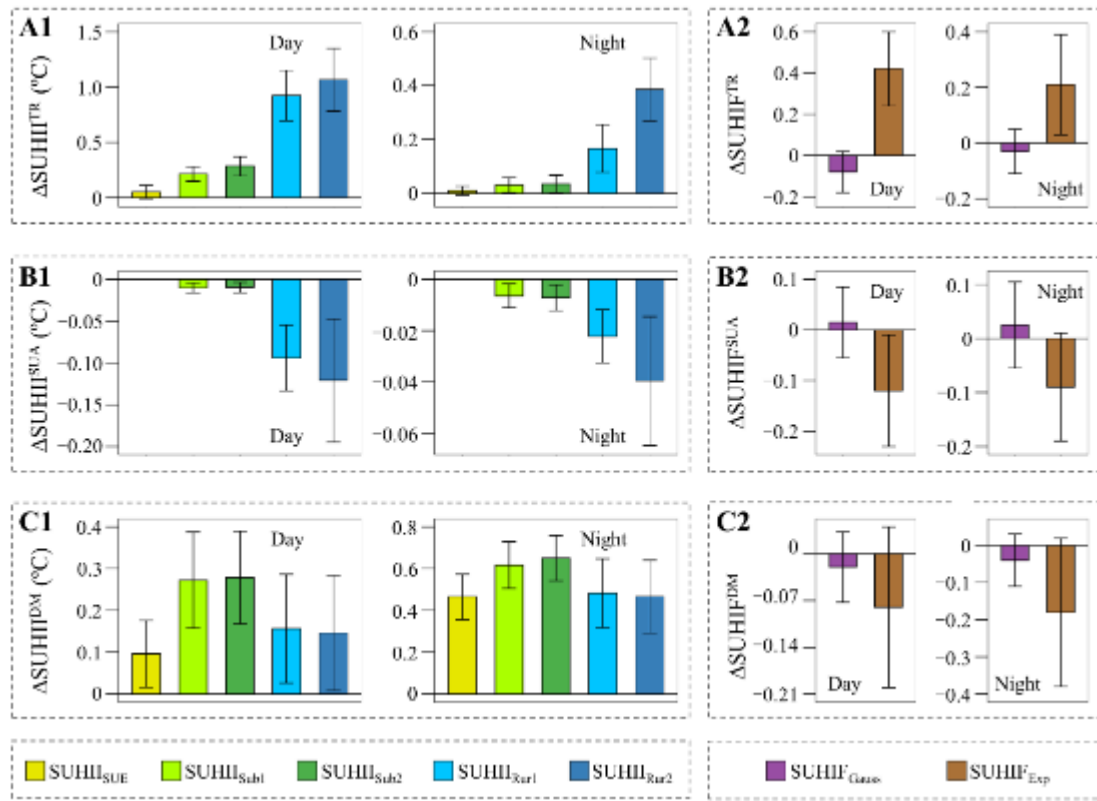


Figure 11. Influence of confounding factors on the SUHI intensity (SUHII) and footprint (SUHIF) for different methods. (A) The average difference in the SUHII ($\Delta SUHII^{TR}$) or SUHIF ($\Delta SUHIF^{TR}$) between that disturbed by topographic relief (TR) and that removed the influence of TR. (B) The average difference in the SUHII ($\Delta SUHII^{SUA}$) or SUHIF ($\Delta SUHIF^{SUA}$) between that disturbed by surrounding urban area (SUA) and that removed the influence of SUA. (C) The average difference in the SUHII ($\Delta SUHII^{DM}$) or SUHIF ($\Delta SUHIF^{DM}$) between that estimated by the original MODIS LST data (disturbed by data missing (DM)) and that estimated by the gap-filled MODIS LST data. The histograms and bars represent the mean values and 95% confidence intervals, respectively. Please refer to Table 1 for details about all the methods.

3.4 Sensitivity to parameters

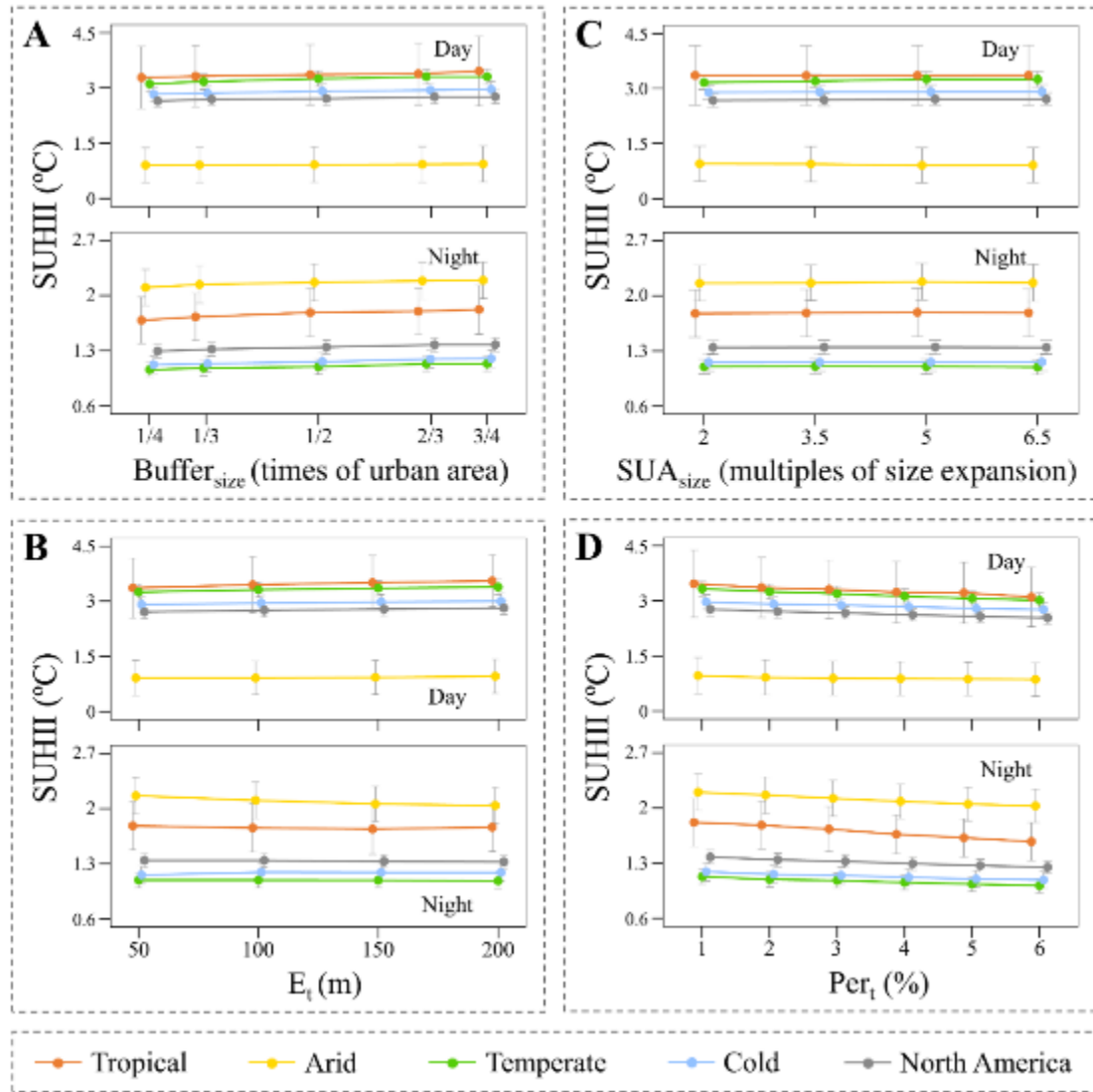


Figure 12. Sensitivity of the SUHII intensity (SUHII) to the parameters of the ASE method. (A) Buffer_{size} is the ratio of the size of each buffer to the size of the central urban area. (B) E_t is the elevation threshold for removing the influence of topographic relief. (C) SUA_{size} is the multiple by which the size of the surrounding urban area is expanded. (D) Per_t is a scaling factor determining the threshold for the extraction of turning points.

Figures 12-13 show the sensitivity of SUHII and SUHIF to each parameter (Buffer_{size}, E_t, SUA_{size}, or Per_t) of the ASE method. Buffer_{size} determines the size of each buffer outside the central urban area, and was set to 1/2 in this study. The increase in Buffer_{size} (from 1/4 to 3/4) causes the urban-rural LST curve to shift outward and become smoother, resulting in the location of TP away from the central urban area

(Figure S4). Correspondingly, higher $\text{Buffer}_{\text{size}}$ corresponds to overall stronger SUHII and SUHIF (Figure 12A-13A). Although SUHIF shows a relatively high sensitivity to $\text{Buffer}_{\text{size}}$, the effect of $\text{Buffer}_{\text{size}}$ appears to be generally consistent across climate zones (Figure 13A).

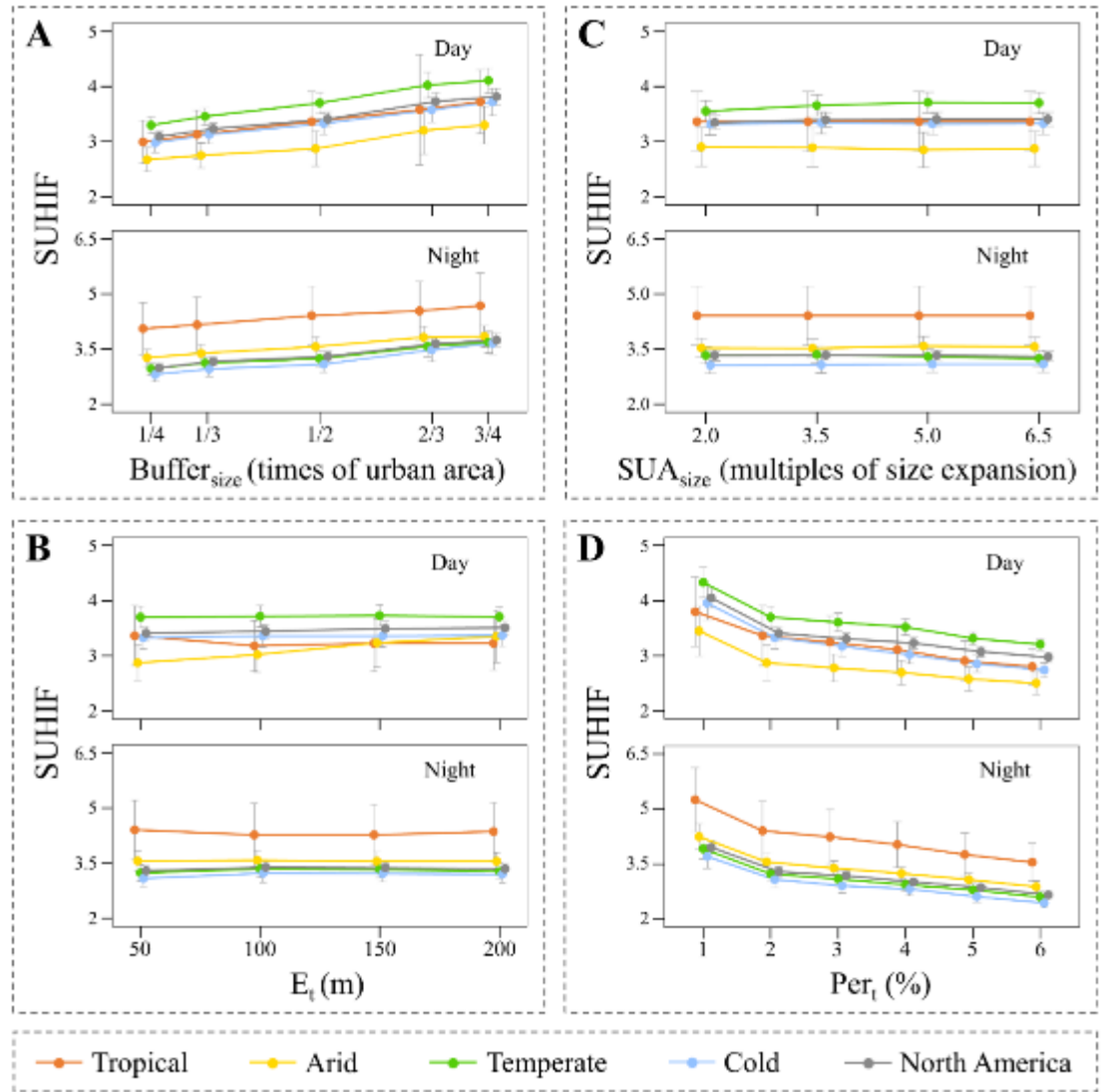


Figure 13. Sensitivity of the SUHI footprint (SUHIF) to the parameters of the ASE method. (A) $\text{Buffer}_{\text{size}}$ is the ratio of the size of each buffer to the size of the central urban area. (B) E_t is the elevation threshold for removing the influence of topographic relief. (C) SUA_{size} is the multiple by which the size of the surrounding urban area is expanded. (D) Per_t is a scaling factor determining the threshold for the extraction of turning points.

In order to minimize the influence of TR and SUA, we set E_t and SUA_{size} to 50 m

and 6.5, respectively, based on relatively strict criteria. For the buffer disturbed by TR, its mean LST tends to decrease with the increase of E_t (from 50 m to 200 m) (Figure S5), resulting in an overall small increase in SUHII (Figure 12B). For the buffer covered by SUAs, the its LST appears to increase with the decrease of SUA_{size} (from 6.5 to 2.0) (Figure S6), resulting in an overall weak decrease in SUHII (Figure 12C). Compared to SUHII, SUHIF seems to be less sensitive to E_t or SUA_{size} (Figure 13B&C).

Per_t is a key parameter for the extraction of the TP, and was set to 2% in this study. It can be seen that as Per_t increases (from 1% to 6%), the TP will gradually approach the central urban area, and the smoother the urban-rural LST curve is, the larger the variation of TP with Per_t (Figure S7). Correspondingly, both SUHII and SUHIF show a decreasing trend with the increase of Per_t , and SUHIF appears to be much more sensitive to Per_t than SUHII (Figures 12D-13D). It is noteworthy that SUHIF decreases substantially when Per_t changes from 1% to 2%, and then the change in SUHIF becomes relatively small (Figure 13D). This also supports, to some extent, our selection of Per_t as 2% in this study.

4. Discussion

4.1 Benefits of the ASE method

(1) The ASE method achieves the simultaneous estimation of SUHI intensity (SUHII) and footprint (SUHIF)

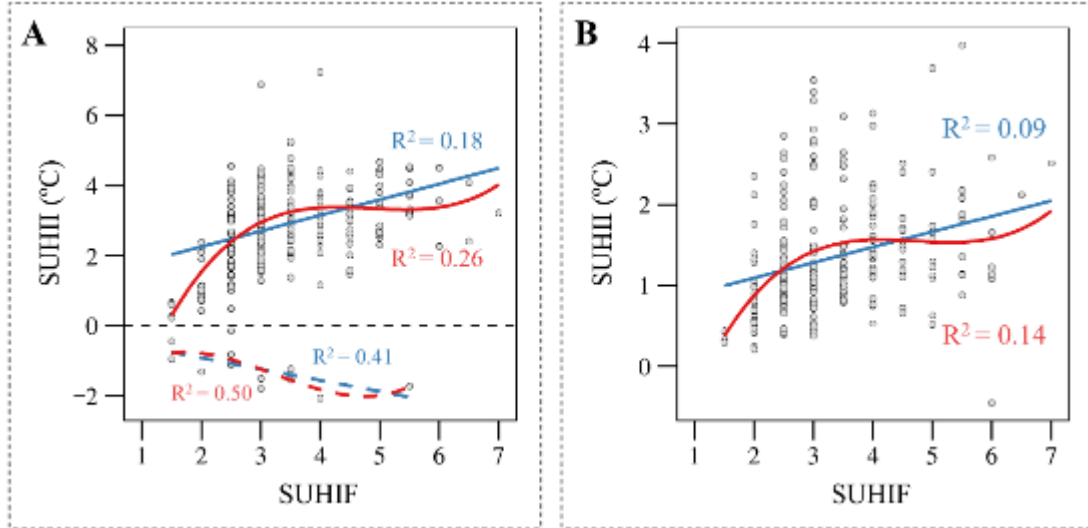


Figure 14. Correlations between the SUHI intensity (SUHI) and the SUHI footprint (SUHIF). (A) Annual daytime results. (B) Annual nighttime results. The blue lines represent the results of linear regression, and the red lines represent the results of nonlinear regression based on cubic equations.

The simultaneous analysis of both SUHI and SUHIF contributes to a comprehensive understanding of the urban heat islands. Firstly, SUHI and SUHIF differ in their definitions, representing two different fundamental properties of the SUHI effect (Hu et al. 2022; Zhou et al. 2018b). By considering both indicators, researchers can gain insights into the average LST differences between urban and rural areas (i.e. SUHI) as well as the spatial extent of the urban thermal influence (i.e. SUHIF). Secondly, SUHI and SUHIF exhibit inconsistencies in terms of spatial distribution, seasonal variation, and day-night differences (see section 3.2), which indicates their distinct nature and behavior within the context of urban heat islands. Thirdly, although there is a statistically positive correlation between SUHI and SUHIF, the correlation is relatively weak and tends to be nonlinear (Figure 14). This further highlights the unique and distinct roles of these two indicators in characterizing the

SUHI effect. Therefore, the ability of the ASE method to obtain both SUHI and SUHIF indicators provides a more holistic perspective on the heat island phenomenon, which facilitates a more thorough examination of its spatiotemporal characteristics and potential driving factors in the future.

(2) The ASE method can adaptively and dynamically select the BRA for estimating the SUHII

It is well-known that identifying the appropriate BRA (i.e. background reference area) is a prerequisite for estimating the SUHII (Li et al. 2022; Zhou et al. 2018b). As shown in Figure 15, LST can vary greatly along the urban-rural gradients, leading to differences in the magnitude (or even opposite signs) of the estimated SUHII when using different BRAs. Given the variations in LST distribution across cities (Figure 3), it is challenging to employ a fixed approach, such as the area-based or distance-based method, for selecting BRAs for all cities. The SUE method, to some extent, gets rid of the difficulty of BRA selection, but still encounters the following issues: (a) It cannot be applied to cities where the entire urban extents consists solely of urban/built-up pixels (Chakraborty and Lee 2019); (b) Its BRA is located adjacent to the urban area and may still be under the influence of the heat island effect (Li et al. 2022), resulting in systematically lower estimated SUHII compared to other methods (Figures 5-6).

The ASE method can adaptively and dynamically select BRA based on the urban-rural LST curves, which has the following advantages over other methods: (a) It extracts BRA based on the characteristics of LST itself, avoiding the arbitrariness in BRA

selection; (b) It can adapt to different cities regardless of the ground cover (see section 4.2); (c) Its BRA is located far away from the central urban area and is not likely to be affected by the heat island effect.

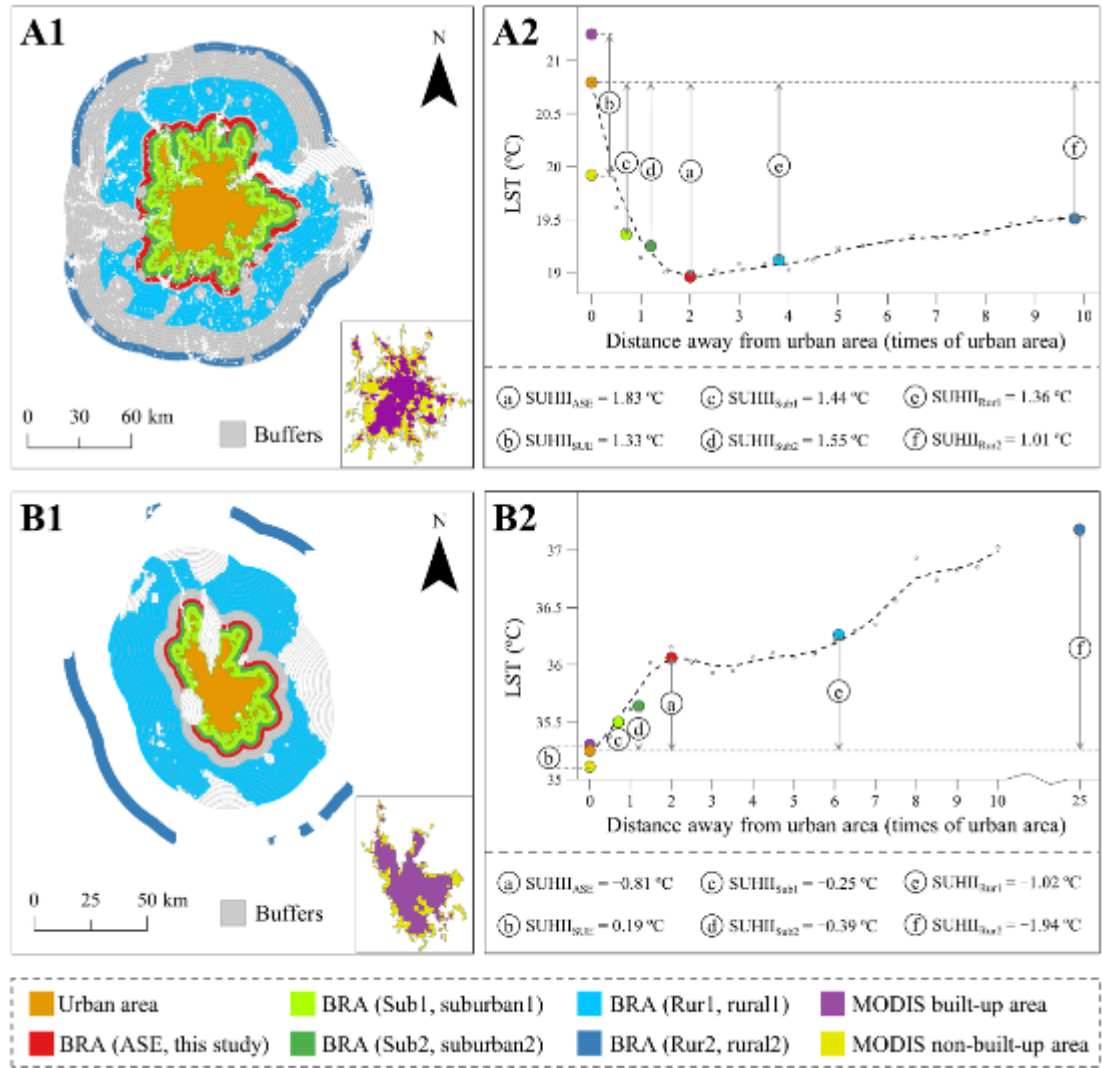


Figure 15. Examples of the background reference area (BRA) and corresponding SUHI intensity (SUHI) of different methods. (A) Kansas City; (B) City of Ciudad Juarez. The BRAs of all methods are located outside of the urban extent, except for the simplified urban-extent (SUE) algorithm, which defines the SUHI intensity as average LST difference between the MODIS built-up and non-built-up areas within the urban extent. Please refer to Table 1 for details about all the methods.

(3) The ASE method avoids the limitations of predefined models in estimating the SUHIF

In terms of the estimation of SUHIF, the Gaussian model is one of the most classic methods, which assumes that the urban LST fits the Gaussian distribution (Hu et al. 2022; Streutker 2003; Yang et al. 2019). The Gaussian model has the ability to derive SUHIF based on the LST spatial continuance, makes it less susceptible to the impacts from data missing (Lai et al. 2021b). Nevertheless, the complexity of urban morphology and LST distribution pose challenges to the practical implementation of the Gaussian model (Anniballe et al. 2014). As exemplified in Figure 16, this method fails to fit the SUHI effect when the LST deviates substantially from the Gaussian distributions. About 20% of the North American cities have encountered this failure when attempting to fit their annual daytime LST using a Gaussian model (Figure 8A).

Unlike the Gaussian model, the ASE method is free from the constrain of the LST distribution and can deal with more complex urban thermal scenarios. Therefore, the ASE method can still achieve effective estimation for SUHIF when the Gaussian model fails (Figure 16). Similar to the Gaussian model, the applicability of other predefined mathematical models (e.g., the exponential model) can also be challenged by the intricate distribution of LST (Zhou et al. 2015). Therefore, the ASE method demonstrates a significant advantage in terms of flexibility compared to the existing predefined mathematical models, and has the potential to estimate the SUHIF in global cities with various LST patterns.

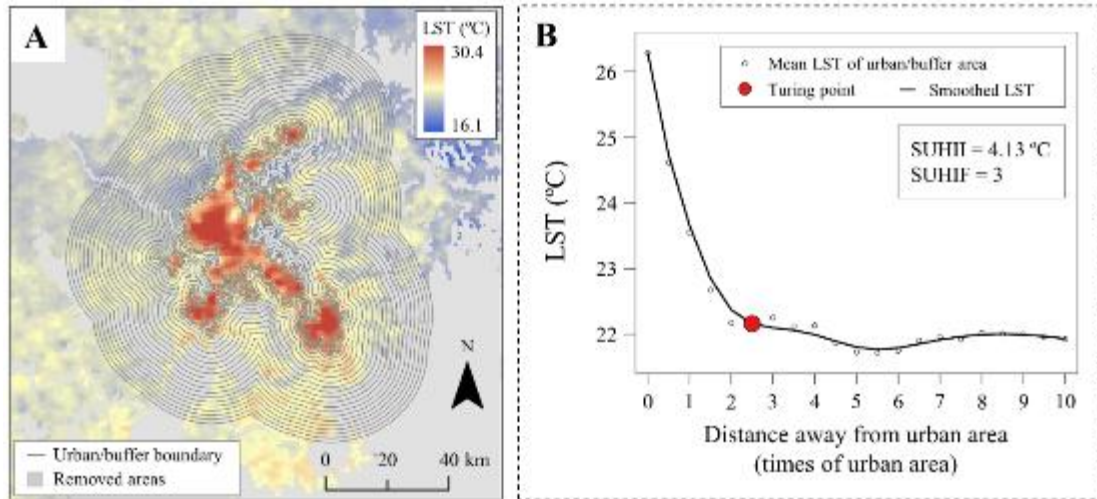


Figure 16. An example of LST that deviate from the Gaussian distribution. (A) Spatial distribution of the annual daytime LST in the city of Nashville. (B) The annual daytime SUHI intensity (SUHII) and footprint (SUHIF) estimated by the ASE method for the city of Nashville.

(4) The ASE method highlights the spatial, seasonal and day-night contrasts of the estimated SUHII

The spatial, seasonal and diurnal patterns of SUHII are important research topics within the field of urban heat island studies (Lai et al. 2018; Liu et al. 2022; Manoli et al. 2019; Yang and Zhao 2023; Zhou et al. 2018b; Zhou et al. 2014). Understanding these patterns can provide valuable insights into the formation and dynamics of urban heat islands and can aid in developing effective strategies to mitigate its effects (Zhou et al. 2018b). The comparison with previous methods indicates that the SUHII estimated by the ASE method exhibits more pronounced spatiotemporal variability. Firstly, The SUHII obtained by the ASE method demonstrates greater spatial heterogeneity, primarily characterized by stronger contrast in average SUHII between different climate zones (Figures 5-6). Secondly, the day-night and summer-winter differences in SUHII, as determined by the ASE method, are substantially higher than

those of the SUE method, moderately stronger than those of the area-based methods, and slightly greater than those of the distance-based methods (Figure 7). Thus, the ASE method can highlight the spatial, seasonal and day-night contrasts of the estimated SUHI intensity. This has the potential to help researchers gain a clearer identification of the spatiotemporal characteristics of the SUHI effect, thereby providing a better understanding of the intricate nature and possible drivers of the urban heat islands (Li et al. 2019a; Manoli et al. 2019; Zhou et al. 2018b).

4.2 Changes in land cover fractions and EVI along urban-rural gradients

Urbanization induces a transition in land cover, generally characterized by a shift from natural features to artificial ones (Liu et al. 2020). This modification in land cover can have an impact on LST, consequently leading to the occurrence of the SUHI effect (Kalnay and Cai 2003; Li et al. 2023; Sun et al. 2016). The ASE method proposed in this study has the capability to extract the BRA by identifying the TP (i.e. turning point) of the urban-rural LST gradients. It is found that the TP of LST varies across cities, which is potentially attributed to the difference in land covers among cities, given the strong association between LST and land covers as revealed by previous studies (Li et al. 2017; Luyssaert et al. 2014; Yang et al. 2021). Therefore, we analyzed the urban-rural changes in the fraction of each land cover (built-ups, bare lands, trees, shrubs, grass, crops) and the enhanced vegetation index (EVI), and extracted their TPs by using the ASE method. Subsequently, we compared the TPs of LST with those of each land cover fraction and the EVI.

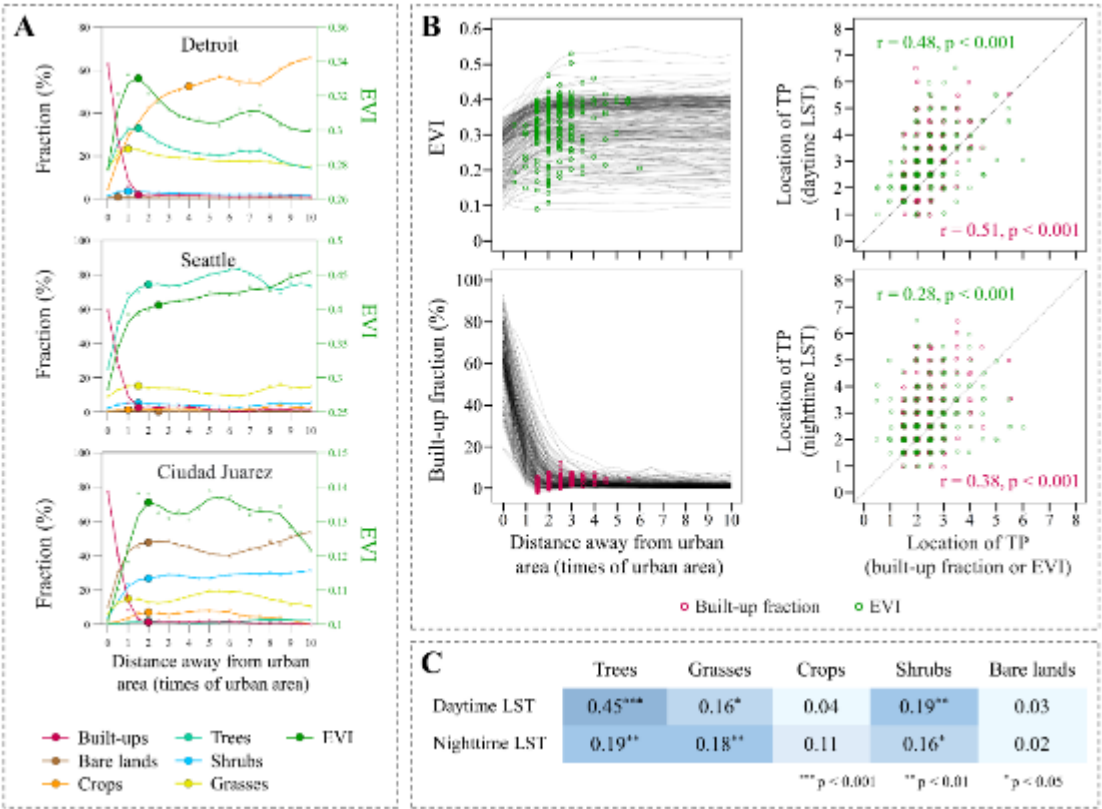


Figure 17. Land cover changes along urban-rural gradients and their correlations with LST. (A) Changes in land cover fractions and the enhanced vegetation index (EVI) along urban-rural gradients and their turning points (TPs), taking 3 cities as examples. (B) The TPs of built-up fraction and EVI and their correlation with those of LST across all North American cities. (C) Pearson correlation coefficients of TPs between LST and the fraction of different land cover.

As shown in Figure 17, the land covers and their variation patterns along urban-rural gradients differ among cities. As the distance from the central urban area increases, there is a decline in the fraction of built-ups, while the fraction of other land covers, i.e. various types of vegetation or bare lands, tends to increase. When the distance from urban areas is significantly large (e.g. reaching the TP), the dominance of built-ups is replaced by other types of land cover, with the specific types varying among cities (Figure 17A). More importantly, the TP of each land cover fraction shows large variations across different cities. Taking the built-up fraction as an example, the TPs are

located at buffers away from the central urban area, with distances ranging from 1.5 to 5.5 times the size of the central urban area (Figure 17B). The decrease in built-ups and the concurrent increase in other land covers contribute to an overall increase in the EVI. The TPs of EVI are located buffers away from the urban area by a distance of 0.5 to 6.5 times the size of urban area, which appear to be more dispersed compared to those of the built-up fraction (Figure 17B). It is found that the TP of LST shows a statistically positive correlation with the TP of land cover fraction and EVI (Figure 17B&C). In comparison, the TP of LST exhibits the strongest correlation with the TP of the built-up fraction, followed by the TP of the EVI, the tree's fraction, and the other land cover fractions. However, even for the built-up fraction and EVI, their corresponding TPs demonstrate notable deviations from those of LST, particularly for the nighttime results (Figure 17B). This indicates that, apart from land cover, there are likely other factors influencing the urban-rural LST distribution.

In summary, the above analysis not only reveals the pattern of land cover change from urban to peripheral, but also further demonstrates the effectiveness and potentials of the ASE method in examining the urban-rural changes. While there is a correlation between the TPs of LST and land covers, the noticeable deviations suggest that the urban-rural LST distribution shall be influenced by multiple factors, and land cover is one of them. Future research should incorporate more data and methods to gain a comprehensive understanding of the influencing factors and their respective contributions in shaping the spatial pattern of urban-rural LST.

4.3 Implications and limitations

This study, by using the innovative ASE method and other methods, provides a comprehensive analysis of the spatiotemporal patterns of SUHII and SUHIF for 254 North American cities. In general, daytime SUHII appears to be low and even negative in most cities located in arid zone, which can be explained by differences in surface energy budget between urban areas and their surroundings for arid cities (Zhao et al. 2014). The area around the city in arid zone usually has less natural vegetation or even is dominated by sand and gravel (Dialesandro et al. 2019; Yang et al. 2021). Moreover, cities in arid regions can be aerodynamically smoother than their arid surroundings leading to additional convective cooling (Li et al. 2019a; Zhao et al. 2014). Overall, urban vegetation, building shadows, and city morphology can all contribute to reducing the urban LST, leading to potential low or negative SUHII. The cold island phenomenon serves as a reminder to be more nuanced about the local environmental consequences of urbanization. Besides, both SUHII and SUHIF show a general temporal pattern that is higher during the day than at night and stronger in summer than in winter. Some studies have suggested some positive feed-backs (e.g. protecting against the extreme cold, reducing heating energy consumption) of wintertime heat island effects (Cui et al. 2017; Li et al. 2019c; Magli et al. 2015; Sun and Augenbroe 2014). However, considering the strong magnitude and large coverage of the summertime SUHI effect, we still need to focus on practicing heat island mitigation measures to cope with the continuously increasing heat stress caused by global warming and climate extremes (Shen et al. 2023), and potentially consider season-aware mitigation measures. Overall,

our proposed ASE method provides an effective way to characterize the spatiotemporal characteristics of the SUHI indicators, which help to further investigate mechanisms and mitigation measures of the urban heat island effect. However, it is also important to keep in mind that although the SUHI has a direct impact on the surface energy budget and potentially on building energy demand, the SUHI magnitude is not equivalent to that of the UHI estimated by air temperature or the urban outdoor heat stress signal (Chakraborty et al. 2022).

Though the ASE method has advantages over existing methods, there are still several potential limitations. First, existing methods are relatively simple for BRA selection, which can be achieved by constructing a single buffer with a predefined distance or area. In contrast, the ASE method is much more complicated for the selection of BRA, which requires not only the construction of multiple buffers, but also the analysis of the urban-rural LST gradients. This leads to a much higher computational complexity of the ASE method than previous methods. However, high-performance and free cloud platforms (e.g., Google Earth Engine, GEE) provide a good opportunity for the global-scale application of the ASE method. Second, the BRA extracted by the ASE method is somewhat related to parameter settings. Though we have discussed the parameter-induced uncertainties through comparative analysis and selected the optimal parameter, we still need to be cautious when interpreting the results of this study. Third, the ASE method is dedicated to identifying appropriate BRA around the central urban areas to achieve effective estimation of SUHI indicators. In fact, the quantification of urban heat islands is also influenced by the extent of the urban area.

Currently, there are numerous global urban area products available, and their urban extents are not always consistent due to difference in definition, data and methods (Huang et al. 2021). Therefore, future research should focus on the uncertainty caused by the differences in urban area delineations.

5. Conclusion

SUHI intensity and footprint are important indicators for measuring the urban thermal environment, capturing the magnitude and spatial extent of the SUHI effect, respectively. Current methods can quantify these two SUHI indicators, but are still challenged by several limitations. Therefore, we proposed the ASE method in this study and analyzed its applicability in 254 North American cities. The comparison reveals several benefits of the ASE method, which can be summarized as follows: (1) The ASE method enables the simultaneous estimation of the SUHI intensity and footprint. This is crucial in providing a more holistic perspective on the SUHI effect, given the weak and nonlinear correlations between the two indicators. (2) The ASE method can adaptively and dynamically select the BRA based on the urban-rural LST curves, which provides a new idea for BRA selection and helps to standardize the estimation of SUHI intensity. (3) The ASE method is not bound by the strict mathematical assumptions, such as Gaussian or exponential models, regarding the distribution of urban LST. This flexibility empowers the ASE method capable of estimating the SUHI footprint for cities with diverse and complex thermal characteristics. (4) The ASE method demonstrates stronger spatial, day-night, and summer-winter differences in the

estimated SUHI intensity. This characteristic underlines its capability to effectively capture the spatiotemporal dynamics of the SUHI effect. Although the ASE method is somewhat sensitive to parameter settings, it generally demonstrates good robustness in its results. Considering the above benefits, the ASE method inspires confidence in its potential to serve as a generalizable tool for quantifying the SUHI effect.

Additionally, we conducted a thorough analysis of the influence of confounding factors, including topographic relief, surrounding urban areas, and LST data missing, on the quantification of the SUHI effect. It is found that ignoring the influence of topographic relief or LST data missing can lead to an overall overestimation of the SUHI intensity, while not removing surrounding urban areas will cause some underestimation of the SUHI intensity. The estimation of SUHI footprint is also affected by these confounding factors, albeit in a more intricate manner. The above results emphasize the necessity of mitigating the influence of confounding factors when quantifying the SUHI effect.

To conclude, this study has introduced the ASE method as an innovative approach to achieve the adaptive and dynamic selection of BAR based on the urban-rural LST gradients. This method enables the synchronous estimation of SUHI intensity and footprint while removing the influence of confounding factors. Despite its apparent complexity compared to existing methods, the ASE method is expected to be applied to long-term and global-scale SUHI studies with the help of cloud computing tools, such as the GEE platform.

Data availability

The global urban boundary (GUB) dataset can be freely available from <http://data.ess.tsinghua.edu.cn/gub.html>. The seamless MODIS Aqua LST products can be publicly downloaded from https://iastate.figshare.com/collections/A_global_seamless_1_km_resolution_daily_land_surface_temperature_dataset_2003_2020_/5078492. All the other data can be accessed from the Google Earth Engine platform (<https://code.earthengine.google.com/>). All data are available upon reasonable request from the authors.

CRedit authorship contribution statement

Qiquan Yang: Conceptualization, Methodology, Software, Investigation, Formal analysis, Visualization, Funding acquisition, Writing - Original Draft, Writing - Review & Editing. **Yi Xu:** Supervision, Funding acquisition, Writing - Review & Editing. **Xiaohua Tong:** Supervision, Funding acquisition, Writing - Review & Editing. **Xin Huang:** Conceptualization, Writing - Review & Editing. **Yue Liu:** Writing - Review & Editing. **TC Chakraborty:** Writing - Review & Editing. **Changjiang Xiao:** Writing-Reviewing and Editing. **Ting Hu:** Writing- Reviewing and Editing.

Acknowledgment

This research was supported by the Macau Young Scholars Program (AM2022001), the China Postdoctoral Science Foundation (2021TQ0245 and 2021M702470), and the

National Natural Science Foundation of China (42201389). The Pacific Northwest National Laboratory is operated for the U.S. Department of Energy (DOE) by Battelle Memorial Institute under contract DE-AC05-76RL01830. T.C.'s contribution was supported by the Regional and Global Modeling and Analysis program area of Coastal Observations, Mechanisms, and Predictions Across Systems and Scales-Great Lakes Modeling (COMPASS-GLM) and Integrated Coastal Modeling (ICoM) projects, both of which are multi-institutional projects supported by DOE's Office of Science's Office of Biological and Environmental Research as part of the Earth and Environmental Systems Modeling program.

References

- Alkama, R., & Cescatti, A. (2016). Biophysical climate impacts of recent changes in global forest cover. *Science*, *351*, 600-604
- Anniballe, R., Bonafoni, S., & Pichierri, M. (2014). Spatial and temporal trends of the surface and air heat island over Milan using MODIS data. *Remote Sensing of Environment*, *150*, 163-171
- Buchhorn, M., Lesiv, M., Tsendbazar, N.-E., Herold, M., Bertels, L., & Smets, B. (2020). Copernicus global land cover layers—collection 2. *Remote Sensing*, *12*, 1044
- Cao, C., Lee, X., Liu, S., Schultz, N., Xiao, W., Zhang, M., & Zhao, L. (2016). Urban heat islands in China enhanced by haze pollution. *Nature Communications*, *7*, 12509

864 Chakraborty, T., & Lee, X. (2019). A simplified urban-extent algorithm to characterize
865 surface urban heat islands on a global scale and examine vegetation control on
866 their spatiotemporal variability. *International Journal of Applied Earth*
867 *Observation and Geoinformation*, 74, 269-280

868 Chakraborty, T., Sarangi, C., & Lee, X. (2021). Reduction in human activity can
869 enhance the urban heat island: Insights from the COVID-19 lockdown.
870 *Environmental Research Letters*, 16, 054060

871 Chakraborty, T., Venter, Z.S., Qian, Y., & Lee, X. (2022). Lower Urban Humidity
872 Moderates Outdoor Heat Stress. *Agu Advances*, 3, e2022AV000729

873 Chen, C., Li, D., & Keenan, T.F. (2021). Enhanced surface urban heat islands due to
874 divergent urban-rural greening trends. *Environmental Research Letters*, 16,
875 124071

876 Cui, F., Hamdi, R., Yuan, X., He, H., Yang, T., Kuang, W., Termonia, P., & De Maeyer,
877 P. (2021). Quantifying the response of surface urban heat island to urban greening
878 in global north megacities. *Science of the Total Environment*, 801, 149553

879 Cui, Y., Yan, D., Hong, T., & Ma, J. (2017). Temporal and spatial characteristics of the
880 urban heat island in Beijing and the impact on building design and energy
881 performance. *Energy*, 130, 286-297

882 De Boor, C., & De Boor, C. (1978). *A practical guide to splines*. springer-verlag New
883 York

884 Dialesandro, J.M., Wheeler, S.M., & Abunnasr, Y. (2019). Urban heat island behaviors
885 in dryland regions. *Environmental Research Communications*, 1, 081005

886 Hu, J., Yang, Y., Zhou, Y., Zhang, T., Ma, Z., & Meng, X. (2022). Spatial patterns and
887 temporal variations of footprint and intensity of surface urban heat island in 141
888 China cities. *Sustainable Cities and Society*, 77, 103585

889 Huang, F., Zhan, W., Wang, Z.-H., Voogt, J., Hu, L., Quan, J., Liu, C., Zhang, N., & Lai,
890 J. (2020). Satellite identification of atmospheric-surface-subsurface urban heat
891 islands under clear sky. *Remote Sensing of Environment*, 250, 112039

892 Huang, X., Cai, Y., & Li, J. (2019). Evidence of the mitigated urban particulate matter
893 island (UPI) effect in China during 2000-2015. *Science of the Total Environment*,
894 660, 1327-1337

895 Huang, X., Huang, J., Wen, D., & Li, J. (2021). An updated MODIS global urban extent
896 product (MGUP) from 2001 to 2018 based on an automated mapping approach.
897 *International Journal of Applied Earth Observation and Geoinformation*, 95,
898 102255

899 Imhoff, M.L., Zhang, P., Wolfe, R.E., & Bounoua, L. (2010). Remote sensing of the
900 urban heat island effect across biomes in the continental USA. *Remote Sensing of*
901 *Environment*, 114, 504-513

902 Jia, W., Zhao, S., & Liu, S. (2018). Vegetation growth enhancement in urban
903 environments of the Conterminous United States. *Global Change Biology*, 24,
904 4084-4094

905 Kalnay, E., & Cai, M. (2003). Impact of urbanization and land-use change on climate.
906 *Nature*, 423, 528

907 Kuang, W., Liu, J., Dong, J., Chi, W., & Zhang, C. (2016). The rapid and massive urban

908 and industrial land expansions in China between 1990 and 2010: A CLUD-based
 909 analysis of their trajectories, patterns, and drivers. *Landscape and Urban*
 910 *Planning*, 145, 21-33

911 Lai, J., Zhan, W., Huang, F., Voogt, J., Bechtel, B., Allen, M., Peng, S., Hong, F., Liu,
 912 Y., & Du, P. (2018). Identification of typical diurnal patterns for clear-sky
 913 climatology of surface urban heat islands. *Remote Sensing of Environment*, 217,
 914 203-220

915 Lai, J., Zhan, W., Quan, J., Liu, Z., Li, L., Huang, F., Hong, F., & Liao, W. (2021a).
 916 Reconciling Debates on the Controls on Surface Urban Heat Island Intensity:
 917 Effects of Scale and Sampling. *Geophysical Research Letters*, 48,
 918 e2021GL094485

919 Lai, J., Zhan, W., Voogt, J., Quan, J., Huang, F., Zhou, J., Bechtel, B., Hu, L., Wang, K.,
 920 Cao, C., & Lee, X. (2021b). Meteorological controls on daily variations of
 921 nighttime surface urban heat islands. *Remote Sensing of Environment*, 253,
 922 112198

923 Li, D., Liao, W., Rigden, A.J., Liu, X., Wang, D., Malyshev, S., & Shevliakova, E.
 924 (2019a). Urban heat island: Aerodynamics or imperviousness? *Science Advances*,
 925 5, eaau4299

926 Li, K., Chen, Y., & Gao, S. (2022). Uncertainty of city-based urban heat island intensity
 927 across 1112 global cities: Background reference and cloud coverage. *Remote*
 928 *Sensing of Environment*, 271, 112898

929 Li, K., Chen, Y., Wang, M., & Gong, A. (2019b). Spatial-temporal variations of surface

930 urban heat island intensity induced by different definitions of rural extents in
931 China. *Science of the Total Environment*, 669, 229-247

932 Li, L., Zhan, W., Hu, L., Chakraborty, T.C., Wang, Z., Fu, P., Wang, D., Liao, W., Huang,
933 F., Fu, H., Li, J., Liu, Z., Du, H., & Wang, S. (2023). Divergent urbanization-
934 induced impacts on global surface urban heat island trends since 1980s. *Remote
935 Sensing of Environment*, 295, 113650

936 Li, W., Cao, Q., Lang, K., & Wu, J. (2017). Linking potential heat source and sink to
937 urban heat island: Heterogeneous effects of landscape pattern on land surface
938 temperature. *Science of the Total Environment*, 586, 457-465

939 Li, X., Gong, P., Zhou, Y., Wang, J., Bai, Y., Chen, B., Hu, T., Xiao, Y., Xu, B., Yang,
940 J., Liu, X., Cai, W., Huang, H., Wu, T., Wang, X., Lin, P., Li, X., Chen, J., He, C.,
941 Li, X., Yu, L., Clinton, N., & Zhu, Z. (2020). Mapping global urban boundaries
942 from the global artificial impervious area (GAIA) data. *Environmental Research
943 Letters*, 15, 094044

944 Li, X., Zhou, Y., Yu, S., Jia, G., Li, H., & Li, W. (2019c). Urban heat island impacts on
945 building energy consumption: A review of approaches and findings. *Energy*, 174,
946 407-419

947 Liao, Y., Shen, X., Zhou, J., Ma, J., Zhang, X., Tang, W., Chen, Y., Ding, L., & Wang,
948 Z. (2022). Surface urban heat island detected by all-weather satellite land surface
949 temperature. *Science of the Total Environment*, 811, 151405

950 Liu, X., Huang, Y., Xu, X., Li, X., Li, X., Ciais, P., Lin, P., Gong, K., Ziegler, A.D.,
951 Chen, A., Gong, P., Chen, J., Hu, G., Chen, Y., Wang, S., Wu, Q., Huang, K., Estes,

952 L., & Zeng, Z. (2020). High-spatiotemporal-resolution mapping of global urban
 953 change from 1985 to 2015. *Nature Sustainability*, 3, 564–570

954 Liu, Z., Zhan, W., Lai, J., Bechtel, B., Lee, X., Hong, F., Li, L., Huang, F., & Li, J.
 955 (2022). Taxonomy of seasonal and diurnal clear-sky climatology of surface urban
 956 heat island dynamics across global cities. *ISPRS Journal of Photogrammetry and*
 957 *Remote Sensing*, 187, 14-33

958 Luyssaert, S., Jammet, M., Stoy, P.C., Estel, S., Pongratz, J., Ceschia, E., Churkina, G.,
 959 Don, A., Erb, K., Ferlicoq, M., Gielen, B., Grünwald, T., Houghton, R.A.,
 960 Klumpp, K., Knohl, A., Kolb, T., Kuemmerle, T., Laurila, T., Lohila, A., Loustau,
 961 D., McGrath, M.J., Meyfroidt, P., Moors, E.J., Naudts, K., Novick, K., Otto, J.,
 962 Pilegaard, K., Pio, C.A., Rambal, S., Rebmann, C., Ryder, J., Suyker, A.E.,
 963 Varlagin, A., Wattenbach, M., & Dolman, A.J. (2014). Land management and
 964 land-cover change have impacts of similar magnitude on surface temperature.
 965 *Nature Climate Change*, 4, 389-393

966 Magli, S., Lodi, C., Lombroso, L., Muscio, A., & Teggi, S. (2015). Analysis of the urban
 967 heat island effects on building energy consumption. *International Journal of*
 968 *Energy and Environmental Engineering*, 6, 91-99

969 Manoli, G., Fatichi, S., Schlapfer, M., Yu, K., Crowther, T.W., Meili, N., Burlando, P.,
 970 Katul, G.G., & Bou-Zeid, E. (2019). Magnitude of urban heat islands largely
 971 explained by climate and population. *Nature*, 573, 55-60

972 Pekel, J.-F., Cottam, A., Gorelick, N., & Belward, A.S. (2016). High-resolution
 973 mapping of global surface water and its long-term changes. *Nature*, 540, 418–422

- 974 Peng, J., Hu, Y., Dong, J., Liu, Q., & Liu, Y. (2020). Quantifying spatial morphology
975 and connectivity of urban heat islands in a megacity: A radius approach. *Science*
976 *of the Total Environment*, 714, 136792
- 977 Peng, J., Ma, J., Liu, Q., Liu, Y., Li, Y., & Yue, Y. (2018). Spatial-temporal change of
978 land surface temperature across 285 cities in China: An urban-rural contrast
979 perspective. *Science of the Total Environment*, 635, 487-497
- 980 Peng, S., Piao, S., Ciais, P., Friedlingstein, P., Ottle, C., Breon, F.M., Nan, H., Zhou, L.,
981 & Myneni, R.B. (2012). Surface urban heat island across 419 global big cities.
982 *Environmental Science & Technology*, 46, 696-703
- 983 Possega, M., Aragão, L., Ruggieri, P., Santo, M.A., & Di Sabatino, S. (2022).
984 Observational evidence of intensified nocturnal urban heat island during
985 heatwaves in European cities. *Environmental Research Letters*, 17
- 986 Qiao, Z., Wu, C., Zhao, D., Xu, X., Yang, J., Feng, L., Sun, Z., & Liu, L. (2019).
987 Determining the Boundary and Probability of Surface Urban Heat Island
988 Footprint Based on a Logistic Model. *Remote Sensing*, 11, 1368
- 989 Quan, J., Chen, Y., Zhan, W., Wang, J., Voogt, J., & Wang, M. (2014). Multi-temporal
990 trajectory of the urban heat island centroid in Beijing, China based on a Gaussian
991 volume model. *Remote Sensing of Environment*, 149, 33-46.
- 992 Rubel, F., & Kotteck, M. (2010). Observed and projected climate shifts 1901–2100
993 depicted by world maps of the Köppen-Geiger climate classification.
994 *Meteorologische Zeitschrift*, 19, 135-141
- 995 Schwarz, N., Lautenbach, S., & Seppelt, R. (2011). Exploring indicators for quantifying

996 surface urban heat islands of European cities with MODIS land surface
 997 temperatures. *Remote Sensing of Environment*, 115, 3175-3186

998 She, Y., Liu, Z., Zhan, W., Lai, J., & Huang, F. (2021). Strong regulation of daily
 999 variations in nighttime surface urban heat islands by meteorological variables
 1000 across global cities. *Environmental Research Letters*, 17, 014049

1001 Shen, P., Zhao, S., Ma, Y., & Liu, S. (2023). Urbanization-induced Earth's surface
 1002 energy alteration and warming: A global spatiotemporal analysis. *Remote Sensing*
 1003 *of Environment*, 284, 113361

1004 Streutker, D. (2003). Satellite-measured growth of the urban heat island of Houston,
 1005 Texas. *Remote Sensing of Environment*, 85, 282-289

1006 Sun, Y., & Augenbroe, G. (2014). Urban heat island effect on energy application studies
 1007 of office buildings. *Energy and Buildings*, 77, 171-179

1008 Sun, Y., Zhang, X., Ren, G., Zwiers, F.W., & Hu, T. (2016). Contribution of urbanization
 1009 to warming in China. *Nature Climate Change*, 6, 706-709

1010 Venter, Z.S., Chakraborty, T., & Lee, X. (2021). Crowdsourced air temperatures
 1011 contrast satellite measures of the urban heat island and its mechanisms. *Science*
 1012 *Advances*, 7, eabb9569

1013 Wang, J., Huang, B., Fu, D., & Atkinson, P. (2015). Spatiotemporal Variation in Surface
 1014 Urban Heat Island Intensity and Associated Determinants across Major Chinese
 1015 Cities. *Remote Sensing*, 7, 3670-3689

1016 Wang, L., De Boeck, H.J., Chen, L., Song, C., Chen, Z., McNulty, S., & Zhang, Z.
 1017 (2022). Urban warming increases the temperature sensitivity of spring vegetation

phenology at 292 cities across China. *Science of the Total Environment*, 834,
155154

Ward, K., Lauf, S., Kleinschmit, B., & Endlicher, W. (2016). Heat waves and urban heat
islands in Europe: A review of relevant drivers. *Science of the Total Environment*,
569, 527-539

Yang, C., & Zhao, S. (2023). Diverse seasonal hysteresis of surface urban heat islands
across Chinese cities: Patterns and drivers. *Remote Sensing of Environment*, 294,
113644

Yang, Q., Huang, X., & Li, J. (2017). Assessing the relationship between surface urban
heat islands and landscape patterns across climatic zones in China. *Scientific
Reports*, 7, 9337-9347

Yang, Q., Huang, X., & Tang, Q. (2019). The footprint of urban heat island effect in
302 Chinese cities: Temporal trends and associated factors. *Science of the Total
Environment*, 655, 652-662

Yang, Q., Huang, X., Yang, J., & Liu, Y. (2021). The relationship between land surface
temperature and artificial impervious surface fraction in 682 global cities:
spatiotemporal variations and drivers. *Environmental Research Letters*, 16,
024032

Yao, R., Wang, L., Huang, X., Gong, W., & Xia, X. (2019). Greening in Rural Areas
Increases the Surface Urban Heat Island Intensity. *Geophysical Research Letters*,
46, 2204-2212

Yao, R., Wang, L., Huang, X., Niu, Y., Chen, Y., & Niu, Z. (2018). The influence of

different data and method on estimating the surface urban heat island intensity.
Ecological Indicators, 89, 45-55

Yao, R., Wang, L., Huang, X., Niu, Z., Liu, F., & Wang, Q. (2017). Temporal trends of
 surface urban heat islands and associated determinants in major Chinese cities.
Science of the Total Environment, 609, 742-754

Zhan, W., Liu, Z., Bechtel, B., Li, J., Lai, J., Fu, H., Li, L., Huang, F., Wang, C., & Chen,
 Y. (2022). Urban-Rural Gradient in Urban Heat Island Variations Responsive to
 Large - Scale Human Activity Changes During Chinese New Year Holiday.
Geophysical Research Letters, 49, e2022GL100689

Zhang, T., Zhou, Y., Zhu, Z., Li, X., & Asrar, G.R. (2022). A global seamless 1 km
 resolution daily land surface temperature dataset (2003–2020). *Earth System
 Science Data*, 14, 651-664

Zhang, X., Friedl, M.A., Schaaf, C.B., Strahler, A.H., & Schneider, A. (2004). The
 footprint of urban climates on vegetation phenology. *Geophysical Research
 Letters*, 31, L12209

Zhao, L., Lee, X., Smith, R.B., & Oleson, K. (2014). Strong contributions of local
 background climate to urban heat islands. *Nature*, 511, 216-219

Zhao, S., Zhou, D., & Liu, S. (2016). Data concurrency is required for estimating urban
 heat island intensity. *Environmental Pollution*, 208, 118-124

Zhou, D., Bonafoni, S., Zhang, L., & Wang, R. (2018a). Remote sensing of the urban
 heat island effect in a highly populated urban agglomeration area in East China.
Science of the Total Environment, 628, 415-429

1062 Zhou, D., Xiao, J., Bonafoni, S., Berger, C., Deilami, K., Zhou, Y., Frolking, S., Yao,
1063 R., Qiao, Z., & Sobrino, J. (2018b). Satellite Remote Sensing of Surface Urban
1064 Heat Islands: Progress, Challenges, and Perspectives. *Remote Sensing*, 11, 48

1065 Zhou, D., Zhang, L., Hao, L., Sun, G., Liu, Y., & Zhu, C. (2016a). Spatiotemporal trends
1066 of urban heat island effect along the urban development intensity gradient in
1067 China. *Science of the Total Environment*, 544, 617-626

1068 Zhou, D., Zhao, S., Liu, S., Zhang, L., & Zhu, C. (2014). Surface urban heat island in
1069 China's 32 major cities: Spatial patterns and drivers. *Remote Sensing of*
1070 *Environment*, 152, 51-61

1071 Zhou, D., Zhao, S., Zhang, L., & Liu, S. (2016b). Remotely sensed assessment of
1072 urbanization effects on vegetation phenology in China's 32 major cities. *Remote*
1073 *Sensing of Environment*, 176, 272-281

1074 Zhou, D., Zhao, S., Zhang, L., Sun, G., & Liu, Y. (2015). The footprint of urban heat
1075 island effect in China. *Scientific Reports*, 5, 11160-11170

1076